CARDIFF UNIVERSITY
PRIFYSGOL CAERDYDD

ORCA – Online Research @ Cardiff

This is an Open Access document downloaded from ORCA, Cardiff University's institutional repository:https://orca.cardiff.ac.uk/id/eprint/177400/

This is the author's version of a work that was submitted to / accepted for publication.

Citation for final published version:

Gleeson, Matthew, Wieser, Penny, DeVitre, Charlotte L., Shi, Sarah C., Millet, Marc-Alban , Muir, Duncan D., Stock, Michael J. and Lissenberg, Johan 2025. Persistent high-pressure magma storage beneath a near-ridge ocean island volcano (Isla Floreana, Galápagos). Journal of Petrology , egaf031. 10.1093/petrology/egaf031

Publishers page: http://dx.doi.org/10.1093/petrology/egaf031

Please note:
Changes made as a result of publishing processes such as copy-editing, formatting and page numbers may not be reflected in this version. For the definitive version of this publication, please refer to the published source. You are advised to consult the publisher's version if you wish to cite this paper.

This version is being made available in accordance with publisher policies. See http://orca.cf.ac.uk/policies.html for usage policies. Copyright and moral rights for publications made available in ORCA are retained by the copyright holders.

Persistent high-pressure magma storage beneath a near-ridge ocean island volcano (Isla Floreana, Galápagos)

Matthew Gleeson[1,2]*, Penny Wieser[1], Charlotte L. DeVitre[1], Sarah C. Shi[1,3], Marc-Alban Millet[2], Duncan D. Muir[2], Michael J. Stock[4], and Johan Lissenberg[2]

[1]Department of Earth and Planetary Science, University of California, Berkeley, McCone Hall, 94720, USA

[2]School of Earth and Environmental Sciences, Cardiff University, Main Building, Park Place, CF10 3AT, UK

[3]Lamont-Doherty Earth Observatory, Columbia University. New York, NY USA

[4]Discipline of Geology, School of Natural Sciences, Trinity College Dublin, Dublin 02, Ireland

*corresponding author contact: gleesonm@berkeley.edu

Keywords: Galapagos Archipelago, gabbro xenoliths, geothermobarometry, fluid inclusions, thermodynamics

ACCEPTED MANUSCRIPT

Downloaded from https://academic.oup.com/petrology/advance-article/doi/10.1093/petrology/egaf031/8102209 by guest on 04 April 2025

© The Author(s) 2025. Published by Oxford University Press. This is an Open Access article distributed under the terms of the Creative Commons Attribution License https://creativecommons.org/licenses/by/4.0/, which permits unrestricted reuse, distribution, and reproduction in any medium, provided the original work is properly cited.

ABSTRACT

Volcanic evolution in ocean island settings is often controlled by variations in the chemistry and volumetric flux of magma from an underlying mantle plume. In locations such as Hawai'i or Réunion, this results in predictable variations in magma chemistry, the rate of volcanic activity, and the depth of magma storage with volcanic age and/or distance from the center of plume upwelling. These systems, however, represent outliers in global plume volcanism due to their high buoyancy flux, frequent eruptions, and large distance from any plate boundary. Most mantle plumes display clear interaction with nearby plate boundaries, influencing the dynamics of solid plume material in the upper mantle and the distribution of melt across regions of active volcanism. Yet, the influence of plume-ridge interaction and plume-ridge distance on the structure, characteristics, and evolution of magma storage beneath ocean island volcanoes remains under constrained. In this study, we consider the evolution of magmatic systems in the Galápagos Archipelago, a region of mantle plume volcanism located 150-250 km south of the Galápagos Spreading Centre (GSC), focusing on the depth of magma storage during the eastward transport of volcanic systems away from the centre of plume upwelling. Geochemical analysis of gabbro xenoliths from Isla Floreana in the south-eastern Galápagos suggest that they formed at ~2-2.5 Ma, when the island was located close to the centre of plume upwelling. These nodules, therefore, provide rare insights into the evolution of volcanic systems in the Galápagos Archipelago, tracking variations in the magma system architecture as the Nazca plate carried Isla Floreana eastwards, away from the plume centre.

Mineral thermobarometry, thermodynamic modelling, and CO_2 fluid inclusion barometry reveal that Isla Floreana's plume-proximal stage of volcanic activity – recorded in the gabbro xenoliths – was characterized by the presence of high-pressure magma storage (> 25 km), below the base of the crust. In fact, we find no petrological evidence that sustained, crustal-level magma storage ever occurred beneath Isla Floreana. Our results contrast with the characteristics of volcanic systems in the western Galápagos above the current centre of plume upwelling, where mid-crust magma

ACCEPTED MANUSCRIPT

Downloaded from https://academic.oup.com/petrology/advance-article/doi/10.1093/petrology/egaf031/8102209 by guest on 04 April 2025

storage has been identified. We propose that this change in magmatic architecture of plume-proximal volcanic centres in the Galápagos – from high-pressure mantle storage at 2.5 Ma to mid-crustal storage at the present day – is controlled by the variations in plume-ridge distance. Owing to the northward migration of the GSC, the distance separating the plume stem and GSC is not constant, and was likely <100 km at 2.5 Ma, significantly less than the current plume-ridge distance of 150 – 250 km. We propose that smaller plume-ridge distances result in greater diversion of plume-material to the GSC, 'starving' the eastern Galápagos islands of magma during their initial formation and restricting the ability for these systems to develop long-lived crustal magma reservoirs.

1 INTRODUCTION

Ocean island volcanoes, primarily formed through melting of anomalously hot, hydrous, or lithologically distinct mantle plumes, represent some of the most active volcanic systems in the world (Harpp and Weis, 2020; Herzberg et al., 2014; Matthews et al., 2021; Métrich et al., 2014; Neal et al., 2019; Sobolev et al., 2007; Weis et al., 2023). Owing to the deep-mantle origin of many mantle plumes, these volcanoes provide a snapshot into the dynamic nature of the Earth's mantle and the origin of large-scale mantle features identified through geophysical techniques (Cabral et al., 2013; Cottaar and Lekic, 2016; French and Romanowicz, 2015; Gleeson et al., 2021; Harpp and Weis, 2020; Jackson et al., 2008; Koppers et al., 2021). In addition, ocean island volcanoes can have significant impacts on local populations, infrastructure, and the global climate (Whitty et al., 2020; Wilson et al., 2014). Despite their scientific and societal importance, uncertainties remain regarding the growth and evolution of ocean island volcanoes, and the interplay between magma chemistry/storage and geodynamic setting (e.g., near-ridge vs intraplate; Cleary et al., 2020a; Geist et al., 2014a; Harpp and Geist, 2018a).

ACCEPTED MANUSCRIPT

Downloaded from https://academic.oup.com/petrology/advance-article/doi/10.1093/petrology/egaf031/8102209 by guest on 04 April 2025

The magmatic architecture and volcanic evolution of ocean island volcanoes has traditionally been studied through petrological analysis of erupted volcanic products (e.g., lava and tephra) and analysis of the geodetic and seismic signatures of volcanic unrest (Bagnardi et al., 2013; Bell et al., 2021; Boudoire et al., 2019; Dayton et al., 2023; DeVitre et al., 2023b; Harpp and Geist, 2018; Neal et al., 2019; Stock et al., 2018). These approaches have demonstrated diversity in the characteristics of ocean island volcanoes, with variations in the composition and temperature of the mantle source, and the flux of magma into the lithosphere translating into dramatic differences in the chemistry and magmatic architecture of the volcanic plumbing systems (Baxter et al., 2023; Baxter and Maclennan, 2024; Geist et al., 2014; Gleeson et al., 2020a; Maclennan, 2019). However, important questions remain, including the influence of geodynamic setting on the architecture of magmatic systems and the evolution of magmatic activity in near-ridge settings (Cleary et al., 2020). In addition, with the growing consensus that magma reservoirs are dominated by crystal-rich, mushy domains, there is increasing recognition that petrological analysis of magmatic cumulates in addition to conventionally-examined erupted material can aid investigation of the chemical, thermal and structural history of ocean island magmatic plumbing systems (Cashman et al., 2017; Gao et al., 2022, 2016; Gleeson et al., 2020a; Horn et al., 2022; Sparks et al., 2019).

At ocean islands, direct access to the cumulate section of the underlying magmatic system is not often available. Instead, snapshots of the underlying mush are provided by cumulate nodules brought to the surface during volcanic eruptions (Clague and Bohrson, 1991; Holness et al., 2019; Lyons et al., 2007). These nodules range from melt-bearing mush fragments to fully solidified xenoliths and typically cover a range of mineralogical assemblages and bulk compositions (Gao et al., 2016; Horn et al., 2022; Stock et al., 2012). In many cases, cumulate xenoliths brought to the surface at post-shield volcanic systems (i.e. downstream of the main region of plume upwelling) record several hundred thousand to millions of years of activity at a single volcanic centre (Clague and Bohrson, 1991; Gao et al., 2016; Lyons et al., 2007). As a result, these cumulate xenoliths not only

ACCEPTED MANUSCRIPT

Downloaded from https://academic.oup.com/petrology/advance-article/doi/10.1093/petrology/egaf031/8102209 by guest on 04 April 2025

provide insights into the architecture of mush-dominated magmatic systems beneath ocean island volcanoes, but also the temporal evolution of the volcanoes from which they are collected.

In this study, we utilize recent developments in the analytical capabilities of Energy Dispersive Spectrometry (EDS) to extract quantitative, multi-scale petrological data from cumulate xenoliths in the Galápagos Archipelago. We couple this with depth constraints from thermodynamic models and fluid inclusion barometry to examine the formation and storage history of these nodules. Specifically, we target Isla Floreana, a low melt-flux volcanic system located in the south-eastern Galápagos where ~2.5 Myr of magmatic activity is recorded in the composition of cumulate nodules found in lava and scoria deposits (Harpp et al., 2014; Lyons et al., 2007). We focus on a suite of gabbroic xenoliths that are hypothesized to have formed when the island was located close to the center of plume upwelling (2 - 2.5 Ma; Gleeson et al., 2020a; Lyons et al., 2007a). Our new data, alongside recent analysis of the present-day Isla Floreana magmatic system (Gleeson et al., 2020a, 2022), is used to evaluate the evolution of an ocean island magmatic system in a near-ridge setting, focusing on the depth of magma storage. Furthermore, comparison of our results to active volcanic centres in the present-day western Galápagos provides insights into the role of geodynamic settings in the construction of magmatic plumbing systems, owing to the migration of the Galápagos mantle plume away from the Galápagos Spreading Centre over the last 5 Myr (Mittelstaedt et al., 2012).

2 GEOLOGICAL BACKGROUND

2.1 VOLCANIC HISTORY AND TECTONIC SETTING

The Galápagos Archipelago, located ~1000 km off the western coast of Ecuador, represents one of the most volcanically active regions in the world. Magmatic activity in the Galápagos is a consequence of adiabatic decompression melting in a chemically and lithologically heterogeneous mantle plume that is likely ~50-150^{o}C hotter than the surrounding ambient mantle (Gibson et al.,

ACCEPTED MANUSCRIPT

Downloaded from https://academic.oup.com/petrology/advance-article/doi/10.1093/petrology/egaf031/8102209 by guest on 04 April 2025

2015; Hooft et al., 2003). Seismic tomography indicates that the current centre of plume upwelling is located beneath the islands of Isabela and Fernandina in the western Galápagos (Fig. 1), which are the most volcanically active islands in the archipelago (eruptions occur every 2-3 years on average; Villagómez et al., 2014). However, historical eruptions have also been documented in the eastern and northern Galápagos, on the islands of Santiago (1759, 1904 - 1906), Pinta (1928) and Marchena (1991), and volcanic activity elsewhere in the eastern Galápagos has been shown to be long-lived (Global Volcanism Program, 2013). For example, volcanic activity on the island of San Cristobal in the eastern Galápagos covers a period of more than 2 Myrs, with the most recent eruption dated at ~9 ka (Mahr et al., 2016). Holocene to late Pleistocene eruptions have also been identified at several of the other eastern Galápagos islands, including Isla Floreana on the southern margin of the archipelago (~26 ka; Harpp et al., 2014a).

The wide geographic distribution of recent volcanic activity in the Galápagos is likely related to variations in lithospheric thickness across the archipelago (Gibson and Geist, 2010), extensional faulting on the eastern islands (Schwartz et al., 2014), and the near-ridge tectonic setting. The Galápagos mantle plume is centered roughly 150 – 250 km south of the east-west trending Galápagos Spreading Centre (GSC), a mid-ocean ridge spreading centre separating the Nazca and Cocos tectonic plates. Transfer of material from the Galápagos plume stem to the GSC (whether in the solid or melt phase) has a clear influence on the composition of erupted basalts along the ridge and may contribute to the volcanism observed in the Northern Galápagos Volcanic Province (Gleeson and Gibson, 2021; Mittal and Richards, 2017).

The distance between the Galápagos mantle plume and the GSC has not been constant over the last 5 Myrs. Owing to the eastward motion of the Nazca tectonic plate and the north-east motion of the Cocos plate, the GSC is migrating north, away from the centre of Galápagos plume upwelling (Mittelstaedt et al., 2012; Wilson and Hey, 1995). In fact, ~5 – 12 Myr ago, the Galápagos mantle plume was likely located directly beneath the GSC, in a tectonic situation analogous to modern

ACCEPTED MANUSCRIPT

Downloaded from https://academic.oup.com/petrology/advance-article/doi/10.1093/petrology/egaf031/8102209 by guest on 04 April 2025

Iceland (Wilson and Hey, 1995). Since then, the separation distance between the mantle plume and spreading center has increased, with its northward migration punctuated by a series of southward ridge-jumps on the eastern GSC (the most recent of which occurred at ~1 Ma) that resulted in the formation of the Galápagos Transform Fault at ~91°W (Mittelstaedt et al., 2012). As a result, when the eastern Galápagos volcanic islands of Floreana and Santa Cruz were first constructed (at around 2 – 3 Ma) the Galápagos mantle plume was located up to ~100 km closer to the GSC than it is at the present day. The 2-3 Myr old eastern Galápagos and the modern western Galápagos, therefore, formed in different geodynamic settings, which might have had a substantial influence on the characteristics of magma storage (Cleary et al., 2020; Harpp and Geist, 2018).

2.2 Variations in volcanic style and morphology

Across the Galápagos Archipelago, there are variations in the style of magmatic activity, which result in key chemical and morphological differences between the various volcanic centres. Broadly, these differences can be used to define two volcanic regions within the Galápagos Archipelago; a western volcanic domain with regular activity focused at 6 central shield volcanoes and an eastern domain with less frequent eruptions and more spatially-distributed eruptive activity (Harpp and Geist, 2018a; Fig. 1).

The western volcanic region, which encompasses the islands of Isabela and Fernandina, is characterized by the presence of 6 large shield volcanoes and the dissected shield of Volcán Ecuador on the northern margin of Isla Isabela (Geist et al., 2014, 2002). These volcanoes range from ~1100 m to ~1700 m in height and are characterized by the presence of a large central caldera and an inverted soup-bowl morphology (Bernard et al., 2019; Geist et al., 2005; Naumann and Geist, 2000; Fig. 1c). The major element, trace element, and isotopic variations observed in erupted material at each of the western volcanic centers is typically relatively narrow (compared to the eastern Galápagos islands), indicating that mantle-derived magmas are efficiently mixed in their magmatic systems and buffered over a narrow range of temperatures by the regular input of new, mantle-

ACCEPTED MANUSCRIPT

Downloaded from https://academic.oup.com/petrology/advance-article/doi/10.1093/petrology/egaf031/8102209 by guest on 04 April 2025

derived magma into the system (Geist et al., 2014, 1995). Recent barometric work, using both petrological and geophysical monitoring data, indicates that the bulk of magma storage occurs in the mid-to-lower crust (7-15 km; Higgins and Stock, 2024; Stock et al., 2018), with a secondary magma storage region present at shallow depths beneath most of the western Galápagos shields (Bagnardi et al., 2013).

The eastern volcanic region encompasses the islands of Santa Cruz, Santa Fe, Floreana, Española, San Cristóbal and Santiago (Harpp and Geist, 2018). These islands are characterized by shallow slope gradients, distributed volcanism, monogenetic scoria cones, and lack of large central edifices (Fig. 1d). There is little to no evidence to indicate the presence of buried calderas beneath the surface of any of the eastern Galápagos islands, which has been presented as evidence that these systems are unlikely to represent the late-stage evolution of a system analogous to the current western Galápagos shield volcanoes (Cleary et al., 2020). Unlike the western Galápagos shield volcanoes, there is a substantial major, trace element and isotopic heterogeneity in the erupted products of each eastern volcanic island (Bow and Geist, 1992; Harpp et al., 2014; Harpp and Geist, 2018). This heterogeneity has been hypothesized to occur due to the lower flux of mantle-derived melts into these islands (relative to the western shields), which is insufficient to form a centralized, thermally buffered mush system capable of homogenizing chemical variations from incoming mantle melts (Gleeson et al., 2020a; Harpp and Geist, 2018). Instead, the magmatic systems are likely ephemeral, poorly connected, and are characterized by a range of melt temperatures and compositions. Melt inclusion and clinopyroxene-based barometry from Isla Floreana, which shows the greatest degree of compositional heterogeneity anywhere in the Galápagos, indicates that magma storage beneath the eastern Galápagos islands is substantially deeper than beneath the western Galápagos shield volcanoes and likely exceeds the depth of the Moho (~16 km; Gleeson et al., 2020a, 2022).

ACCEPTED MANUSCRIPT

Downloaded from https://academic.oup.com/petrology/advance-article/doi/10.1093/petrology/egaf031/8102209 by guest on 04 April 2025

2.3 GALÁPAGOS PLUME HETEROGENEITY

The wide distribution of Holocene and late Pleistocene volcanism in the Galápagos has been used to unravel the compositional heterogeneity in the upwelling mantle plume (Geist et al., 1988; White et al., 1993). Several different mantle components have been identified or proposed, including enriched mantle reservoirs with highly radiogenic Pb and Sr isotope ratios (most prominently seen on Isla Floreana; Harpp et al., 2014a; White et al., 1993), primordial mantle domains retaining unradiogenic He isotope signatures ($^3He/^4He$ up to ~29 R/R_A; Isla Fernandina; Kurz et al., 2009; Kurz and Geist, 1999), and a depleted component whose origin (intrinsic plume material vs entrained upper mantle) remains debated (Gibson et al., 2012; Harpp and White, 2001; Hoernle et al., 2000).

Overall, at least 4 chemically and/or lithologically distinct components have been proposed (Geist et al., 1988; Gleeson et al., 2021, 2020b; Gleeson and Gibson, 2019; Harpp and White, 2001; Vidito et al., 2013). These components have a complex spatial arrangement that is long-lived on timescales of several 10s of Myrs (Hoernle et al., 2000). At the most basic level, the Galápagos can be split into an isotopically depleted north-eastern domain – where basalts have isotopic signatures that are similar to the global MORB field – and an isotopically enriched south-western domain (Gleeson et al., 2021; Harpp and Weis, 2020). The boundary separating these two domains is sub-parallel to the boundary separating the western and eastern volcanic regions (yellow line, Fig. 1a). As a result, Volcán Wolf on northern Isabela falls within the western volcanic region (Harpp and Geist, 2018), but is chemically more closely related to volcanic systems in the north-eastern Galápagos (Harpp and Weis, 2020). Conversely, Isla Floreana in the southern Galápagos forms part of the eastern volcanic region (gentle slopes and an abundance of monogenetic scoria cones) yet displays the most radiogenic Sr and Pb isotope signatures of any volcanic island in the Galápagos and is thus associated with the chemically enriched south-western domain (Gleeson et al., 2020a; Harpp et al., 2014; Harpp and Weis, 2020).

The chemical asymmetry of the Galápagos Archipelago is similar to the presence of the Loa and Kea geochemical trends in Hawai'i (Harpp and Weis, 2020). The main difference between the two

ACCEPTED MANUSCRIPT

Downloaded from https://academic.oup.com/petrology/advance-article/doi/10.1093/petrology/egaf031/8102209 by guest on 04 April 2025

systems is that the chemical asymmetry in the Galápagos is not orientated parallel to the direction of plate motion. As this chemical asymmetry in the Galápagos is long-lived on timescales >15 Myrs (Hoernle et al., 2000), the isotopic and trace element composition of erupted material at the surface of each individual volcanic system will change through time as the Nazca Plate moves east-southeast above the mantle plume. The anticipated chemical evolution of any particular volcanic system is controlled by the position of the volcano with respect to latitude; for example, in a central strip spanning west to east across the archipelago (e.g., Isla Fernandina, Volcán Alcedo, Isla Pinzón, and Isla Santa Cruz) the mantle source region will move across the boundary separating the enriched south-western domain and the depleted north-eastern domain leading to a temporal progression from enriched to depleted isotopic signatures (Wilson et al., 2022). In contrast, along the southern margin of the Galápagos platform (Volcán Cerro Azul, Volcán Sierra Negra, and Isla Floreana) the west-to-east progression is characterized by variations in the degree of enrichment and differences in key trace element and isotopic parameters (Fig. 1). Specifically, Isla Floreana basalts contain more radiogenic Sr and Pb isotope signatures relative to Volcán Cerro Azul and Volcán Sierra Negra, as well as offsets in many trace element ratios (e.g., $[Sm/Yb]_n$, where n indicates normalization to the primitive mantle estimate of Sun and McDonough, 1989; Fig. 1; Harpp et al., 2014a). Consequently, volcanic evolution over millions of years at the southern margin of the Galápagos platform – the region targeted in this study – should be associated with a systematic shift to more enriched isotopic signatures and concave Rare Earth Element patterns (high $[La/Sm]_n$ but low $[Sm/Yb]_n$ ratios).

3 METHODS

The gabbroic xenoliths analysed in this study represent 2 – 5 cm diameter nodules collected from scoria cones in the north-east corner of Isla Floreana (17MMSG03b, 17MMSG04b; hereafter 03b and 4b) and small fragments (exposed areas of ~0.5-3 cm^2) found in the core of a blocky lava flow near Punta Cormorant on Isla Floreana's northern coast (17MMSG09; Fig. 1). Prior to analysis, all samples

ACCEPTED MANUSCRIPT

Downloaded from https://academic.oup.com/petrology/advance-article/doi/10.1093/petrology/egaf031/8102209 by guest on 04 April 2025

were cut into small blocks <1 cm thick with exposed areas ranging from <0.5 – 5 cm^2. Lava samples containing small gabbroic fragments (17MMSG09; hereafter 09g1, 09g2, and 09g3) were cut to maximize the surface exposure of the gabbro. The cut samples were ground down using various grades of silicon carbide grit and then prepared for analysis by polishing the exposed surface areas with a 1 µm diamond suspension.

3.1 FEG-SEM ANALYSIS

The polished gabbroic blocks were carbon coated to a thickness of ~10 - 13 nm and analyzed using both the Zeiss Sigma HD Field Emission Gun Scanning Electron Microscope (FEG-SEM) at Cardiff University School of Earth and Environmental Science and the JEOL JSM IT800HL FEG-SEM at the University of California, Berkeley. Analyses were performed over a range of length-scales, from whole-sample compositional maps to high-precision analysis of major and minor elements in linescans and individual point analyses.

3.1.1 Quantitative compositional mapping

Quantitative compositional maps of the exposed gabbroic regions were produced for all samples using the Cardiff Zeiss Sigma HD FEG-SEM and two Oxford Instruments X-Max 150 Energy Dispersive Spectrometers. Maps were created with a pixel size of 25 X 25 µm using a beam current of ~1.1 nA (determined through the choice of aperture size – 60 µm) and an accelerating voltage of 20 kV. To reduce background noise and increase spectral resolution, the signal process time was set to the AZtec preset 3 (~2 microseconds per X-ray). The dwell time was 0.05 seconds for each pixel, and a quantitative chemical composition was generated using a predefined calibration file (determined through analysis of mineral and metal standards; see Supplementary Material), and a XPP matrix correction routine (implemented through the associated AZtec software).

To assess the accuracy and precision of our map data, 15 mineral standards were mapped within the same analytical session as our gabbroic xenoliths. The estimated concentrations of all elements >2

ACCEPTED MANUSCRIPT

Downloaded from https://academic.oup.com/petrology/advance-article/doi/10.1093/petrology/egaf031/8102209 by guest on 04 April 2025

wt% are typically within 2% of the published standard value. Relative offsets between predicted and published values for oxides with lower concentrations are larger, in part owing to uncertainties in the published standard compositions and the presence of minor element heterogeneity within these samples. The analytical precision for each pixel was low (relative 1σ precision of >39% for Na in Diopside – Astimex standard), but is substantially improved by binning multiple pixels. For example, generating 1000 compositions of each mapped standard by averaging the composition of 25 pixels in a randomly selected 5-by-5 grid indicates that the analytical precision of Na in Diopside (concentration of 0.3 wt%) in this binned region is ~7.5% (calculated as the relative 1σ value). For elements present in concentrations > 1 wt% (e.g., Ca in Diopside), the analytical precision for each pixel is between 10% and 2%, improving to 3% to <1% for a 5-by-5 pixel region.

3.1.2 Map Data processing

Quantitative EDS mapping provides a wealth of information for each of the gabbroic xenoliths. Using this data, we can identify the major phases within a sample, constrain the compositional distribution of each phase, and determine the bulk sample composition. We used the Python3 package mineralML to identify the major phases present in each sample (Shi et al., 2023). mineralML uses Bayesian neural networks, trained on over 86,000 analyses of 17 minerals (data compiled from literature) and validated upon ~1 million analyses (data from EarthChem, GEOROC, and LEPR), to predict the mineral phase for each chemical composition provided (i.e., every map pixel). mineralML also supplies the probability of classification for each analysis; we filter out pixels where the predicted probability is less than 0.6. The primary effect of this filtering step is the removal of pixels whose analytical totals are < 90 wt%, typically representing cracks and/or holes where high-quality analyses were not possible.

Once the mineral abundances and mean compositions have been determined (Fig. 2; Supplementary Information) a 'bulk-rock' composition can also be calculated by determining the weighted average of all pixels assigned a phase by mineralML:

ACCEPTED MANUSCRIPT

Downloaded from https://academic.oup.com/petrology/advance-article/doi/10.1093/petrology/egaf031/8102209 by guest on 04 April 2025

$$C = \frac{\sum_{i=0}^{n} C_i \times \rho_i}{\sum_{i=0}^{n} \rho_i}$$

Where C represents the bulk concentration of the chosen oxide; C_i indicates the measured concentration in pixel i; and ρ_i represents the estimated density of the mineral located at each pixel (based on the identified mineral phase; see Supplementary Material). To estimate the uncertainty associated with these bulk concentration estimates, we generate 200 possible compositions for samples 03b and 04b where an area accounting for >33% of the total sample were randomly selected for each calculation. In general, the uncertainties estimated by this method are very low, typically less than 2% (relative 1σ variation) for most oxides.

We consider the compositions estimated from samples 03b and 04b to be representative of their bulk-rock compositions. This is supported by the similarity between the SEM-derived bulk-rock estimates presented here and the bulk-composition of other Isla Floreana gabbros previously determined by XRF analysis (Lyons et al., 2007; see Supplementary Material). Furthermore, our error analysis indicates that samples 03b and 04b are homogeneous on scales smaller than the analyzed areas (see Supplementary Material). Nevertheless, we caution that the composition of samples 09g1, 09g2, and 09g3 must be treated with care, as these samples are characterized by relatively small areas (<0.5 cm^2), and the presence of heterogeneity on scales smaller than the pixel resolution of our large-scale maps (see below).

3.1.3 Qualitative, high-resolution chemical mapping

To supplement the large-scale maps and provide more information about any small-scale heterogeneity within each sample, qualitative chemical maps of orthopyroxene-clinopyroxene grain boundaries were also collected on the Cardiff Zeiss Sigma HD FEG-SEM. No standards were mapped alongside these high-resolution maps and so quantitative chemical compositions were not calculated. Each map was collected under identical analytical conditions to the large-scale maps, but with a pixel size of 1.5 X 1.5 µm (Fig. 3).

ACCEPTED MANUSCRIPT

Downloaded from https://academic.oup.com/petrology/advance-article/doi/10.1093/petrology/egaf031/8102209 by guest on 04 April 2025

3.1.4 Linescans

In addition to the qualitative maps of clinopyroxene-orthopyroxene grain boundaries, EDS linescans were collected, using the Zeiss Sigma HD FEG-SEM and 2 X-Max EDS detectors, to provide quantitative chemical information of these regions. Five passes, with a dwell time of 3 seconds per spot on each pass, were carried out along each line (ranging from 140 to 220 µm in length with a spatial resolution of 1.5 µm). Data collection was performed using a 1.1 nA beam current, a 20 kV accelerating voltage, and a process time of 3 (AZtec preset value). Quantification was performed using the same calibration file that was used for individual spot analyses (see Supplementary File), which was constructed using point analyses of a range of mineral and metal standards. To check the accuracy and precision of analyses, linescans were also performed on two clinopyroxene standards. Data from these standards indicate that the precision of analyses ranges from ~5% (1σ relative standard deviation) for minor components such as Al_2O_3 and Na_2O (0.6 wt% and 0.41 wt% respectively) to <0.5% (1σ relative standard deviation) for SiO_2 and CaO. Measured compositions of the secondary standard materials are typically within 1% of the preferred standard values.

3.1.5 Point Analyses

In addition to compositional maps and linescans, we perform high-precision point analyses of clinopyroxene, orthopyroxene and plagioclase crystals in all the Isla Floreana gabbros. The major and minor element composition of pyroxene crystals was determined through EDS analysis (using two X-Max 150 detectors) on the Cardiff Zeiss Sigma HD FEG-SEM. For these analyses, the beam was rastered over an area of 1 µm by 1.5 µm and analyses were performed using a 1.1 nA beam current and a 20 kV accelerating voltage. As with the compositional maps and EDS linescans, the process time was set as the AZtec preset 3, and a 15 second live dwell time was used for all EDS point analyses. The EDS calibration file was constructed via analyses of appropriate mineral and metal standards (see Supplementary Material and Supplementary Datasets 1 & 2).

ACCEPTED MANUSCRIPT

Downloaded from https://academic.oup.com/petrology/advance-article/doi/10.1093/petrology/egaf031/8102209 by guest on 04 April 2025

The composition of plagioclase crystals hosted in the Isla Floreana gabbros was determined through EDS-WDS (Wavelength Dispersive Spectrometry) analysis on the JEOL JSM IT800HL FEG-SEM at UC Berkeley. The JEOL FEG-SEM provides a greater range in possible beam conditions than the Zeiss SigmaHD FEG-SEM in Cardiff, providing access to higher beam currents (~100 nA) suitable for minor element analysis by WDS. The concentration of most major and minor elements in the plagioclase crystals (i.e., SiO_2, Al_2O_3, FeO_t, CaO, Na_2O, and K_2O) was determined through EDS analysis using a single Ultim-Max 100 mm^2 detector. During analysis the beam was rastered over a 1-by-1.5 µm area using a beam current of 2 nA and an accelerating voltage of 20kV. The process time for these analyses was set at the Aztec process time 5 (~10 microseconds). Following EDS analyses the beam current was increased to 100 nA and the concentration of MgO (and K_2O in some crystals), at the location of each EDS analysis, was determined via WDS using an Oxford Instruments Wave detector. Counts of Mg were collected for 40 seconds on peak using a TAP crystal, and background counts were collected for 20 seconds on either side of the peak. When measured, counts of K were also collected with a 40 second peak count time and 2*20 second background count time using a PET crystal. Analysis of MgO and K_2O via WDS were calibrated through analysis (at 10nA) of a synthetic Forsterite standard and an Orthoclase standard, respectively.

Analyses of secondary standard materials, including clinopyroxene, plagioclase and garnet, were performed at regular intervals (~2 – 3 hours) to determine the accuracy and precision of analyses (see Supplement for full list of standard sources). These data demonstrate that our EDS analysis is typically accurate to within 1% for high concentration elements (i.e., > 2 wt%) within the secondary standard materials. Outputted error estimates (determined by the Aztec software), and the variability in the estimated composition of secondary standard materials, indicates that the 1σ relative precision of all EDS analyses is <0.5 - 1 % for elements present in high concentrations (> 2 wt%) and increases to ~10-15% for analyses of minor elements (0.2 – 1 wt%). The relative 1σ precision of WDS analyses is estimated to be <3% for MgO in plagioclase (at ~0.12 wt%) and <1.5% for K_2O (at 0.12 wt%). For all analyses we consider the detection limit to equivalent to 3σ.

ACCEPTED MANUSCRIPT

Downloaded from https://academic.oup.com/petrology/advance-article/doi/10.1093/petrology/egaf031/8102209 by guest on 04 April 2025

3.2 Laser Ablation Inductively Coupled Plasma Mass Spectrometry

Clinopyroxene trace element abundances were determined using an ASI RESOlution 193 nm Laser Ablation system coupled to an Agilent 8900 triple quadrupole ICP-MS hosted in the CELTIC laboratory at Cardiff University. Data was collected for 2 minutes per analysis, including a 20 second delay prior to laser initiation, 60 seconds of data collection with the laser active, and a 40 second wash-out period. A 4.5 J/cm^2 fluence, a 10 Hz repetition rate, and an 80 µm spot size was used for all analyses.

Data processing was carried out using the LaserTram software (Lubbers et al., 2021) with BCR-2g as the calibration standard. ^{43}Ca was used as the internal standard for all analyses and the accuracy of analysis was tracked through regular measurements of multiple secondary standards (Jochum et al., 2005). These analyses indicate that all elements reported here return values within ~5% of the published standard values. The relative 1σ precision of analysis is typically <2 – 3% for most elements, although it is important to note that the concentration of most trace elements in the clinopyroxene unknowns are substantially lower than those in the glass secondary standards. Repeat analysis of clinopyroxene cores from our gabbroic samples indicates that the relative 1σ analytical precision is <5% for all light and middle Rare Earth Elements (REEs), increasing to ~8 – 10% for the heavy REEs (see Supplementary Dataset 3).

3.3 Fluid Inclusion Analysis

The density of CO_2 in fluid inclusions (FIs) can provide a powerful barometer in CO_2-dominated magmatic systems as CO_2 density is strongly related to the pressure and relatively insensitive to temperature (Hansteen and Klügel, 2008; Wieser et al., 2025). We quantify CO_2 densities in clinopyroxene and plagioclase-hosted FIs using microthermometry and calibrated Raman Spectroscopy following the methods of DeVitre and Wieser (2024). To isolate crystals containing FIs we carefully cut a small section (~5 mm x 5 mm x 1mm) of samples 03b and 04b following

ACCEPTED MANUSCRIPT

Downloaded from https://academic.oup.com/petrology/advance-article/doi/10.1093/petrology/egaf031/8102209 by guest on 04 April 2025

completion of EDS chemical analysis. These sections were then crushed and individual clinopyroxene and plagioclase crystals were picked from the crushed material and examined for the presence of FIs. These crystals were mounted in crystal bond and ground down using 1200 and 2500 grade silicon carbide paper. Crystals with visible fluid inclusions were then polished using 10000 grade paper and 1μm 3M polishing paper before they were flipped and polished on the other side. Once a thin wafer (< 300 μm) had been prepared with FIs clearly visible within ~100 μm of the surface, crystals were extracted from the crystal bond using a hot plate and Acetone and placed into separate vials. We primarily target fluid inclusions with no visible evidence of decrepitation. Most fluid inclusions in sample 04b appear as isolated inclusions with no clear connection to trails or fracture planes and are thus labelled as 'apparent primary fluid inclusions'. Many of the inclusions measured in 03b are interpreted as secondary as they are located in trails (see Supplementary Material for full textural characterization).

Heating and cooling experiments were performed on a Linkam THMSG600 heating and freezing stage at UC Berkeley. Temperature was calibrated using the melting temperature of a pure H_2O fluid inclusion (0°C) and the melting temperature of CO_2 (-56.6 °C) in a H_2O-CO_2 fluid inclusion. We recorded the melting point/interval and homogenization temperature of each fluid inclusion with a precision of ~+/- 0.1^{o}C using the cycling technique (Hansteen and Klügel, 2008). Homogenization temperatures were converted into CO_2 densities using equations 3.14 and 3.15 of Span and Wagner (1996), implemented in DiadFit (Wieser and DeVitre, 2024).

We also analyzed all fluid inclusions from sample 04b by calibrated Raman spectroscopy, following the methods of DeVitre and Wieser (2024). In summary, we utilize a WiTec Alpha 300R Raman spectrometer at the Department of Earth and Planetary Sciences at the UC Berkeley, with a green 532.046 nm laser and an 1800 grating. Accounting for the small and variable size of fluid inclusions, we use 50-100X objectives for analysis. Laser powers of 6 mW were used throughout to minimize the effects of laser heating (DeVitre et al., 2023a; Hagiwara et al., 2019). Instrument drift was

ACCEPTED MANUSCRIPT

Downloaded from https://academic.oup.com/petrology/advance-article/doi/10.1093/petrology/egaf031/8102209 by guest on 04 April 2025

corrected using the ~1117 and 1447 cm^{-1} Ne emission lines (see DeVitre and Wieser, 2024; Lamadrid et al., 2017). All peak fitting was performed in the Python3 tool DiadFit (Wieser and DeVitre, 2024; see Supplementary Dataset 4). The CO_2 densities determined through Raman Spectroscopy and Microthermometry are typically equivalent within analytical uncertainties, consistent with prior work (DeVitre and Wieser, 2024). To check for the presence of other gaseous species that may have contributed to the derivation in observed melting temperatures from the theorectical melting point of CO_2 (e.g., CO, CH_4, N_2), we analyzed fluid inclusion covering the complete range of observed melting temperatures at higher laser power (49 mW) and a 300 grating, resulting in higher signal strength and a wider range of wavenumbers recorded in a single acquisition.

To calculate pressure from the density of CO_2 in a fluid inclusion using the CO_2 equation of state, an estimate of the entrapment temperature is required. Fluid inclusion pressures will likely relax via diffusion creep during prolonged storage and cooling of the system (Hansteen and Klügel, 2008; Wanamaker and Evans, 1989) to equilibrate internal and external pressures. Consequently, under the assumption of full re-equilibration, we use the temperatures derived from clinopyroxene-orthopyroxene thermobarometry and Mg-in-plagioclase thermometry to invert the measured homogenization temperatures and calculated CO_2 densities into pressure. These calculations were performed using the CO2 EOS of Span and Wagner (1996), implemented in CoolProp (Bell et al., 2014), and accessed through DiadFit (Wieser and DeVitre, 2024). Further calculations were performed to investigate the potential influence of H_2O, He, and Ar on the calculated pressures (see Supplementary Material).

ACCEPTED MANUSCRIPT

Downloaded from https://academic.oup.com/petrology/advance-article/doi/10.1093/petrology/egaf031/8102209 by guest on 04 April 2025

4 RESULTS & DISCUSSION

4.1 MINERALOGICAL & CHEMICAL SIGNATURES IN THE CONTEXT OF GALÁPAGOS VOLCANISM

All gabbro samples considered here display a high degree of textural equilibrium, with 120° grain boundary angles at plagioclase triple junctions and a narrow range in grain sizes (mean size ~500 μm; Gleeson et al., 2020a). While these textures restrict petrographic characterization of the xenoliths based on their original igneous texture (i.e., forming through mechanical settling vs. in situ crystallization) estimated bulk-rock compositions derived from the EDS maps are consistent with that expected from crystal fractionation (i.e., the residual solid assemblage), with density sorted settling of plagioclase and mafic mineral phases in a liquid-rich reservoir resulting in the observed compositional variations (see Supplementary Information).

EDS maps and associated phase predictions from mineralML also reveal a consistent mineralogical signature across our Isla Floreana gabbros (2 pyroxene + plagioclase + spinel) with no residual melt. All samples are dominated by plagioclase (32 – 69%) and clinopyroxene (22 – 49%), with lower proportions of orthopyroxene (1 – 16%) and an Al-rich spinel (typically < 5%; Fig. 2). No olivine is identified in samples 03b and 04b, with only a small number of olivine pixels (associated with orthopyroxene rims) in samples 09g1 – 3 (Fig. 2, 3). High-resolution chemical maps of the orthopyroxene grain boundaries confirm the presence of these inferred olivine pixels, revealing small crystals of olivine forming in orthopyroxene breakdown rims (Fig. 3). Consequently, the presence of minor olivine in samples 09g1-3 is unlikely to represent the equilibrium mineral assemblage, indicating that all 5 samples considered here display essentially the same mineralogy. This is consistent with the mineralogy reported for gabbroic xenoliths collected from Isla Floreana by Lyons et al. (2007a), with substantial olivine only reported in samples with high MgO contents (> 20 wt%).

ACCEPTED MANUSCRIPT

Downloaded from https://academic.oup.com/petrology/advance-article/doi/10.1093/petrology/egaf031/8102209 by guest on 04 April 2025

457 The abundant plagioclase in our samples is, however, at odds with many petrographic and
458 geochemical characteristics of Isla Floreana lavas. Plagioclase is absent or only present as a minor
459 phase in most lavas exposed at the surface of Isla Floreana (< 1.5 Ma), and may represent
460 disaggregated xenolith material where it does occur (Gleeson et al., 2020a; Harpp et al., 2014).
461 Similarly, most lavas on Isla Floreana are olivine-phyric, a phase conspicuously absent from our
462 xenolith samples. Furthermore, erupted lava whole-rock major element trends – such as negatively
463 correlated Al_2O_3 vs MgO contents – indicate that erupted lava compositions are controlled by
464 crystallization or addition of olivine and minor clinopyroxene, with plagioclase playing little to no
465 role in the evolution of the Isla Floreana magmas (Harpp et al., 2014).

466 The differences between the Isla Floreana gabbros and the recent Isla Floreana magmatic system
467 (detailed by Gleeson et al. (2022, 2020a)) extend beyond the mineralogy of these xenoliths. The
468 composition of the clinopyroxene crystals found in the Isla Floreana gabbros contrasts with the
469 composition of crystals collected from scoria cones and lava flows that are not associated with any
470 xenolith group (termed 'autocrysts' by Gleeson et al., 2020a). The gabbroic clinopyroxenes are
471 characterized by relatively low Mg# (where Mg# = Mg/(Mg+Fe) molar), with crystals in samples
472 09g1-3 averaging Mg# ~0.77, slightly lower than those measured in samples 04b (~0.79) and 03b
473 (~0.81; Fig. 4). By contrast, autocrystic clinopyroxenes measured in the Isla Floreana lavas typically
474 have Mg# between 0.84 and 0.90 (Fig. 4).

475 In addition, the trace element signature of the gabbroic clinopyroxene crystals are distinct from
476 those measured in other clinopyroxene groups from Isla Floreana (autocrysts, wehrlite and dunite
477 xenoliths; Gleeson et al., 2020a). The primitive mantle normalized REE patterns of the gabbro
478 clinopyroxenes display a positive light-to-middle REE slope, and a negative slope from the middle to
479 heavy REEs (Fig. 5). This pattern is expressed by the high $[Sm/Yb]_n$ ratios measured in the gabbroic
480 clinopyroxenes (>1.7; where 'n' symbolizes normalization to the primitive mantle values of Sun and
481 McDonough, 1989), which are significantly higher than those measured in the other clinopyroxene

ACCEPTED MANUSCRIPT

Downloaded from https://academic.oup.com/petrology/advance-article/doi/10.1093/petrology/egaf031/8102209 by guest on 04 April 2025

groups (1 – 1.5; Fig. 5b,c). When converted into equilibrium melt compositions, using the parameterization of Sun and Liang (2012), our new clinopyroxene data exceed the measured $[Sm/Yb]_n$ ratio of any basalt erupted on the surface of Isla Floreana (Fig. 6). Taken together, these data indicate that the gabbroic xenoliths found in scoria and lava deposits on Isla Floreana are unlikely to have formed from crystallization of their carrier liquid, or any magma composition that is related to basaltic compositions currently exposed on the surface of the island.

Prior work has revealed that the present style of volcanism on Isla Floreana (i.e., infrequent eruption of olivine-physic basalts) has lasted for around 1 – 1.5 Myrs (Harpp et al., 2014). As the gabbro xenoliths show no clear geochemical relationship to this 'recent' period of volcanism on Isla Floreana, it is necessary to consider other possible origins. For example, at other ocean island volcanoes worldwide (e.g., Hualalai, Hawai'i; Gao et al., 2022), trace element and isotopic signatures have been used to identify the presence of gabbro xenoliths originating from the underlying oceanic crust. However, xenoliths of gabbroic cumulates associated with the Nazca oceanic crust (that are unrelated to Galapagos plume volcanism) would be expected to have very different chemical and mineralogical characteristics to those observed in the Isla Floreana gabbros. Most importantly, the clinopyroxene trace element (e.g., high $[La/Yb]_n$ and $[Sm/Yb]_n$ ratios) and radiogenic isotope systematics (from Lyons et al. 2007) confirm that the Isla Floreana gabbros must be formed by magmas generated at high pressure in the Galapagos mantle plume and cannot be associated with periods of ridge volcanism.

Consequently, we consider possible formation of these gabbros during an earlier period of Isla Floreana's magmatic history, prior to the period of current volcanism starting at ~1.5 Ma. At ~2 – 2.5 Ma Isla Floreana was located close to the present-day position of Volcán Cerro Azul, near the centre of plume upwelling owing to the west-to-east motion of the Nazca tectonic plate (Argus et al., 2011; Harpp et al., 2014). Lavas erupted at western Galápagos shield volcanoes, including Volcán Cerro Azul, are typically plagioclase-phyric (Geist et al., 2002; Naumann and Geist, 2000), possess

ACCEPTED MANUSCRIPT

Downloaded from https://academic.oup.com/petrology/advance-article/doi/10.1093/petrology/egaf031/8102209 by guest on 04 April 2025

overlapping clinopyroxene Mg# and plagioclase An compositions with the Isla Floreana gabbros (Stock et al., 2020, 2018). They also possess high melt $[Sm/Yb]_n$ contents (Gibson and Geist, 2010) – indicating high pressure melting in the plume centre – that overlap with the equilibrium melt values predicted from the Isla Floreana gabbros (Fig. 6). In addition, radiogenic isotope data from a separate suite of Isla Floreana gabbros reveal Sr, Nd, and Hf isotope compositions that are distinct from the erupted Isla Floreana basalts, but overlap with the compositions measured from basalts in the western Galapagos (Volcán Cerro Azul and Volcán Sierra Negra). As a result, we propose that the Isla Floreana gabbros likely originate from a 'plume proximal' stage of Isla Floreana's magmatic history when the island was located close the centre of plume upwelling – near the present-day location of Volcán Cerro Azul – at around 2-2.5 Ma.

The proposed age of these xenoliths is also supported by the EDS maps and linescans, which can identify the degree of chemical heterogeneity and zoning within individual crystal phases. Chemical zoning – be it concentric, patchy, or oscillatory – is a common feature of plagioclase and clinopyroxene crystals in volcanic and plutonic environments worldwide (Bennett et al., 2019; Lissenberg and MacLeod, 2016; Sanfilippo et al., 2020). Our data, however, indicates almost complete homogeneity across each crystal phase with only smooth core-rim zoning of An contents identified in some plagioclase crystals (see Supplementary Material). This indicates that there has been sufficient time for chemical diffusion to smooth (or remove) any chemical zoning, even for the slowest diffusing elements. For example, EDS linescans reveal an absence of zoning in minor components of clinopyroxene (e.g., Ti) over length scales of ~100 μm, an observation in consistent with late-stage crystallization of magma within a cumulate mush (Lissenberg et al. 2016 and others). Assuming a temperature of 1000°C and diffusivities from Cherniak and Liang, (2012) simple calculations of diffusive length scales (i.e., $x = \sqrt{(4Dt)}$) indicate that homogenization over these distances likely require timescales more than 350,000 kyrs. Furthermore, Ca-Na interdiffusion in plagioclase is often considered to be negligible in volcanic systems due to the extremely low diffusivities ($D_{Ca-Na}^{plag} \sim 7 * 10^{-25}\ m^2/s$ at 1000°C and $\sim 2 * 10^{-21}\ m^2/s$ at 1250°C; Grove et al.,

ACCEPTED MANUSCRIPT

Downloaded from https://academic.oup.com/petrology/advance-article/doi/10.1093/petrology/egaf031/8102209 by guest on 04 April 2025

1984). Nevertheless, given the ~2 Myr timescale proposed here, these diffusivities equate to Ca-Na diffusion length scales in plagioclase between 15 and 750 μm. Even at the lower end of this range these distances are consistent with diffusive 'smoothing' of any original An zoning in plagioclase crystals during cooling of these xenoliths, consistent to the gentle core-rim profiles observed in a subset of crystals. Combined with the high degree of textural equilibrium observed in the Isla Floreana gabbros (Gleeson et al., 2020a) this chemical homogeneity supports the proposed long-term storage of these samples and their origin within an ancient (~2 – 2.5 Myr) magmatic system beneath Isla Floreana.

4.2 THERMODYNAMIC CONSTRAINTS ON CUMULATE STORAGE AND SUBSOLIDUS HISTORY

The mineralogy, trace element composition, and isotopic signature of the Isla Floreana gabbros links these samples to the plume-proximal stage of the island's magmatic history at 2-2.5 Ma. However, there are several features within the Isla Floreana gabbros that contrast with the petrographic and chemical characteristics of the modern-day plume-proximal volcanic systems (e.g., Cerro Azul; Gleeson et al., 2020a; Harpp et al., 2014; Lyons et al., 2007; Naumann and Geist, 2000) and may provide insights into the storage conditions, and subsolidus history of these cumulate xenoliths.

The first difference lies in the absence of a stable olivine phase in the gabbros and the presence of orthopyroxene (Fig. 2). All shield volcanoes in the current western Galápagos erupt lavas saturated in some combination of olivine, clinopyroxene, and plagioclase (plus minor oxide phases), with orthopyroxene rare or absent (Geist et al., 2002; Naumann and Geist, 1999; Reynolds and Geist, 1995). In contrast, all gabbros considered here contain abundant orthopyroxene macrocrysts (>5%), but no stable olivine. Furthermore, the clinopyroxene crystals in Isla Floreana gabbros contain anomalously high Na_2O contents (0.72 – 0.89 wt%) relative to data from volcanic systems in the western Galápagos (Fig. 4; Stock et al., 2020, 2018). Offsets are also seen in the clinopyroxene trace element contents. For example, our gabbroic clinopyroxenes contain clear Eu anomalies (defined as

ACCEPTED MANUSCRIPT

Downloaded from https://academic.oup.com/petrology/advance-article/doi/10.1093/petrology/egaf031/8102209 by guest on 04 April 2025

557 $Eu^* = \frac{Eu_n}{\sqrt{Sm_n + Gd_n}}$), ranging from ~1.15 – 1.35 in samples 03b and 04b, to 1.4 – 1.6 in samples 09g1,
558 09g2, and 09g3 (Fig. 5). Similar Eu* values are not seen in any other clinopyroxene data from Isla
559 Floreana (Fig. 5; Gleeson et al., 2020a) and while clinopyroxene trace element data is not available
560 for any western Galápagos shield volcano, the Eu* values of erupted lavas in the western Galápagos
561 does not exceed 1.1 (using compiled data from Gleeson et al., 2021 and Harpp and Weis, 2020).

562 As the Isla Floreana gabbros contain little chemical heterogeneity (i.e., an absence of chemical
563 zoning) and high extents of textural equilibrium have previously been reported (Gleeson et al.,
564 2020a), we hypothesize that the unusual chemical and mineralogical signatures of the Isla Floreana
565 gabbros might result from chemical reactions that take place as the systems transition into
566 equilibrium subsolidus assemblages. To investigate this, we use estimated whole-rock compositions
567 from the EDS maps as inputs to thermodynamic models calibrated for sub-solidus igneous systems
568 to examine the chemical and mineralogical changes that would occur during subsolidus cooling of
569 cumulates. We use the Python3 package PetThermoTools (Gleeson & Wieser, 2024) to create phase
570 diagrams for samples 03b and 04b using the pMELTS (Ghiorso et al., 2002), and Holland et al. (2018)
571 thermodynamic models, implemented through alphaMELTS and MAGEMin (Riel et al., 2022; Smith
572 and Asimow, 2005).

573 Results using the pMELTS thermodynamic model are shown in Fig. 7. The pMELTS simulations
574 indicate that olivine is stable in these samples at pressure below ~750 MPa at 950°C, increasing to
575 800 – 850 MPa at the solidus (1200 – 1250°C). Garnet – also absent from our samples – is predicted
576 to be stable at pressures >750 MPa at 950°C, increasing to >1100 MPa at the solidus. Consequently,
577 it is only between these phase boundaries (olivine-out and garnet-in reactions), at temperatures
578 above 950°C, where our observed mineral assemblage is predicted to be stable (Fig. 7). This
579 indicates a final pressure of equilibration for these gabbros >750 MPa, far greater than the pressures
580 expected at the base of the crust beneath Isla Floreana (~380-450 MPa; Feighner and Richards,
581 1994, using their assumed density of 2800 kg/m^3 for the crust). Calculations performed using the

ACCEPTED MANUSCRIPT

Downloaded from https://academic.oup.com/petrology/advance-article/doi/10.1093/petrology/egaf031/8102209 by guest on 04 April 2025

582 Holland et al. (2018) thermodynamic models, however, predict greater pressures for the garnet-in
583 and olivine-out reaction boundaries. For example, the olivine-out phase reaction occurs between
584 ~800 and 900 MPa for the Holland et al. (2018) thermodynamic model (see Supplementary
585 Information).

586 In addition to estimating the final storage pressure of these cumulates, the pMELTS phase diagrams
587 also provide insights into the phase reactions that occur during subsolidus cooling. For example, our
588 phase calculations indicate that orthopyroxene is not stable at or above the solidus. In fact,
589 assuming these gabbro nodules originated as a cumulate mush (melt + crystals), the initial cumulus
590 phases were likely clinopyroxene + plagioclase + olivine +/- spinel, consistent with the cumulus
591 assemblage predicted for active volcanic systems in the western Galápagos where orthopyroxene is
592 rarely observed (Geist et al., 2002; Naumann and Geist, 1999; Stock et al., 2020). The presence of
593 orthopyroxene therefore supports our hypothesis that significant chemical and mineralogical
594 changes occurred during subsolidus cooling, which we examine in more detail using two possible
595 subsolidus cooling models.

596 In the first model we assume that the system starts at the solidus at a pressure of 800 MPa and
597 undergoes isobaric cooling to a temperature of 1020^{o}C (Fig. 8) based on clinopyroxene-
598 orthopyroxene thermobarometry. In our second model, we assume the solidified gabbroic mush
599 zone undergoes an initial period of isobaric cooling at lower pressure, followed by a period of burial
600 (increasing pressure) due to emplacement of lava/intrusions at shallower levels (Fig. 8). This second
601 model is similar to that proposed by Lyons et al. (2007) and assumes emplacement of ~5 km of lava
602 or shallow level intrusions following initial formation of the gabbro cumulates (approximately half of
603 the total thickness of the Galápagos Platform). Ultimately, this leads to an increase in the system
604 pressure from ~670 MPa to 800 MPa.

605 For both samples considered here the two models demonstrate a sequence of phase changes during
606 cooling (and burial) that can be simplified as:

ACCEPTED MANUSCRIPT

Downloaded from https://academic.oup.com/petrology/advance-article/doi/10.1093/petrology/egaf031/8102209 by guest on 04 April 2025

$$plagioclase + olivine \rightarrow spinel + orthopyroxene\ (+clinopyroxene)$$

The decrease in the modal proportion of olivine and plagioclase in these samples during cooling (and pressurization, Fig. 8) requires a re-distribution of Na, Sr, and Eu – elements that are dominantly found in plagioclase – into other mineral phases. Our models reveal an increase in the Na_2O content of clinopyroxene during cooling (by a factor of ~1.6-1.8X; Fig. 8). While MELTS cannot model Sr-Eu partitioning directly, we propose that these sub-solidus reactions may also be responsible for the strong positive Eu anomalies found in the gabbroic clinopyroxenes. Interestingly, in the subsolidus cooling models there is a decrease in the clinopyroxene TiO_2 content, consistent with the slightly lower concentration of TiO_2 in the gabbro clinopyroxenes compared to data from Volcán Wolf (Fig. 4).

The thermodynamic models also provide a potential explanation for the presence of olivine crystals in orthopyroxene breakdown rims of samples 09g1-3, identified through high-resolution EDS mapping paired with automated mineral classification by mineral ML (Fig. 3). The stability of orthopyroxene is highly sensitive to pressure (Fig. 7), with replacement of orthopyroxene by olivine predicted to occur during depressurization. We suggest that the breakdown rims formed during ascent and decompression of these nodules either shortly prior to, or during eruption. What remains uncertain is why breakdown rims are observed in the 09g samples, but not in 03b and 04b. One important difference between the sample groups is that 03b and 04b were collected from explosively emplaced scoria cones, whereas 09g were found within the centre of a blocky lava flow. This could suggest that variations in ascent rate and/or surface cooling timescales could influence the formation of these orthopyroxene break-down rims.

4.3 Formation and Storage depths

One of the key predictions from the thermodynamic modelling described above is that the absence of olivine in these gabbros requires pressures greater than that found at the Moho, and thus

ACCEPTED MANUSCRIPT

Downloaded from https://academic.oup.com/petrology/advance-article/doi/10.1093/petrology/egaf031/8102209 by guest on 04 April 2025

formation and/or storage below the base of the oceanic crust (Fig. 7). The thermodynamic modelling does, however, contain significant uncertainties that are difficult to fully quantify or demonstrate (including the offset between different models, the uncertainty in bulk-rock estimates, and the oxygen fugacity/water content of the subsolidus system). To more rigorously assess the pressure of gabbro formation and storage beneath Isla Floreana, we consider the available independent barometric evidence from both mineral chemistry and fluid inclusion CO_2 densities.

4.3.1 Mineral Thermobarometry

Due to the presence of subsolidus equilibration in the Isla Floreana gabbros, widely used melt-based thermobarometers (e.g., Cpx-Liq) and single-phase thermobarometers that were calibrated on mineral-melt pairs (e.g. Cpx-only) cannot be applied to our samples (Gleeson et al., 2020a). However, thermobarometers based on equilibria between different solid phases might provide first order constraints on the pressure of gabbro storage and, more importantly, constrain the system temperature (a necessary input parameter for converting fluid inclusion measurements into pressure estimates). For example, the temperature dependent exchange of Mg (coupled with Ca) between clinopyroxene and plagioclase holds a lot of promise for sub-solidus mafic systems and has previously been used to evaluate the cooling history of oceanic gabbros (Faak et al., 2014; Sun and Lissenberg, 2018).

Plagioclase compositions for the gabbroic xenoliths, determined through coupled EDS (Si, Al, Ca, Na, Fe) and WDS (Mg, K) analysis, show little variability within each sample (both core and rim analyses were performed for each crystal). Samples 09g1-3 have low Anorthite contents (An = Ca/(Ca+Na+K) *molar*), ranging from 0.625 (09g1) to 0.643 (09g3), and moderately high K_2O contents around 0.163 – 0.191 wt% (Fig. 9). Sample 04b is characterized by substantially higher An values (~0.76), with sample 03b displaying intermediate compositions (~0.67 – 0.69; Fig. 9). Samples 03b and 04b also show lower K_2O contents than the 09g gabbros 0.061 – 0.112 wt%. Notably, the An-K_2O relationships in the gabbroic plagioclase closely mirrors that observed in plagioclase data from Volcán Wolf,

ACCEPTED MANUSCRIPT

Downloaded from https://academic.oup.com/petrology/advance-article/doi/10.1093/petrology/egaf031/8102209 by guest on 04 April 2025

chosen as a characteristic volcanic system in the western Galápagos due to the abundance of mineral data available (Fig. 9b; Stock et al., 2020). The MgO contents measured in the gabbroic plagioclase are, however, substantially lower than the bulk of the data from Volcán Wolf. Samples 09g1, 09g2, and 09g3 contain average MgO contents of 0.032 wt%, 0.027 wt%, and 0.024 wt%, respectively (Fig. 9c). These values are lower than those measured in samples 03b and 04b (0.038 wt% and 0.037 wt%, respectively).

These plagioclase MgO contents, combined with EDS analysis of clinopyroxene crystals in the same samples (to determine the Mg partition coefficient $K_{Mg} = {Mg_{Plag}}/{Mg_{Cpx}}$), can be used to evaluate the storage temperature of the Isla Floreana gabbros. To evaluate the uncertainty on our temperature calculations, we use a Monte Carlo approach to propagate the analytical error associated with the plagioclase MgO and An contents, and mean clinopyroxene MgO contents. For each analysis and each parameter, we generate 2000 samples from a normal distribution with a standard deviation defined by the either the 1 sigma analytical uncertainty (e.g., plagioclase MgO contents) or the 1 sigma variation in measured composition (e.g., the mean clinopyroxene MgO contents). As the parameterization is also pressure sensitive, we incorporate uncertainty in pressure using a uniform distribution spanning 0.2 and 0.8 GPa, the previously determined range in magma storage conditions for Galápagos basalts (Bell et al., 2021; Gleeson et al., 2020a; Stock et al., 2018). The mean temperature estimated for each individual plagioclase analysis varies from 913.2°C (±22.0°C) to 997.0°C (±11.5°C; Fig. 9d).

In addition to the Mg in plagioclase thermometer, the temperature and pressure of the system can be estimated using the composition of co-existing clinopyroxene and orthopyroxene crystals (Putirka, 2008). Importantly, EDS linescans reveal no compositional zoning in either clinopyroxene or orthopyroxene crystals near the grain boundaries, indicating complete chemical equilibration between these phases at their subsolidus storage conditions. To evaluate the role of analytical uncertainties on the precision of our 2-pyroxene thermobarometric calculations we generated 200

ACCEPTED MANUSCRIPT

Downloaded from https://academic.oup.com/petrology/advance-article/doi/10.1093/petrology/egaf031/8102209 by guest on 04 April 2025

680 hypothetical clinopyroxene/orthopyroxene compositions for each EDS analysis using Thermobar (3 –
681 5 analyses taken per crystal Wieser et al., 2022). These compositions were determined by assuming
682 a normal distribution of probabilities centered on the measured oxide concentration (i.e., the mean
683 of the distribution) with a standard deviation set by the estimated error of analysis. For each
684 clinopyroxene-orthopyroxene pair this process resulted in 600 – 1000 paired compositions that were
685 used to calculate the temperature and pressure of storage. Calculations were performed by iterating
686 the results of equations 36 & 38 and equations 36 & 39 from Putirka (2008), implemented in the
687 Python3 package Thermobar (Wieser et al., 2022).

688 Temperatures determined through clinopyroxene-orthopyroxene thermobarometry, iterating
689 equation 36 (temperature) with equation 38 (pressure) from Putirka (2008), range from 1042.3^{o}C
690 (±18.9^{o}C) for sample 04b to 1014.4^{o}C (±11.4^{o}C) in sample 09g1 (Fig. 10). If equation 39 is used to
691 determine the system pressure, the mean temperature estimated for each sample decreases by
692 approximately 10-20^{o}C. Overall, our results indicate that clinopyroxene-orthopyroxene equilibrium
693 in the Isla Floreana gabbros records temperatures at the upper end of those estimated by Mg-in-
694 plagioclase thermometry, but with smaller uncertainties. At present, the cause of the offset between
695 the two methods is not clear, but the region of overlap between the two methods indicates that
696 storage at >900^{o}C is likely for the Isla Floreana gabbros (Fig. 10).

697 Application of clinopyroxene-orthopyroxene equilibria to determining the pressure of gabbro
698 storage is, however, associated with significant uncertainty due to the large variation in estimated
699 pressures associated with different equation pairs. If equation 39 is iterated with equation 36 to
700 simultaneously solve for pressure and temperature our data indicates storage around 627 ±59 MPa
701 (sample 04b) to 678 ±42 MPa (sample 03b). If we instead use equation 38 (which is independent of
702 temperature) to determine the system pressure, we get estimates of 940 ±102 MPa and 886 ±72
703 MPa for samples 04b and 03b (Fig. 10). The large difference between the two barometric equations
704 indicates that there is a large degree of uncertainty in these pressure calculations. Considering the

ACCEPTED MANUSCRIPT

Downloaded from https://academic.oup.com/petrology/advance-article/doi/10.1093/petrology/egaf031/8102209 by guest on 04 April 2025

95% confidence 'envelope' on a P-T plot (calculated using the Python3 package pyrolite; Williams et al., 2020) reveals a small region of overlap between the two clinopyroxene-orthopyroxene pressure-temperature calculations at ~750 MPa and 1000 – 1025°C (Fig. 10). However, given the difference between the two equations, and the uncertainties estimated for each approach, all we can realistically conclude from clinopyroxene-orthopyroxene barometry is that these gabbros were likely stored at pressures higher than ~450 MPa, representing the maximum possible pressure at the base of the oceanic crust beneath the Galápagos Platform (calculated using the crustal thickness estimate of Feighner and Richards (1994a) and a constant crustal density of 2800 kg/m^3).

4.3.2 Fluid Inclusion Barometry

Both thermodynamic simulations and clinopyroxene-orthopyroxene barometry indicate that the gabbro xenoliths were stored at >450 MPa, below the base of the Galápagos crust. Unlike mineral thermobarometers, which are relatively imprecise (e.g. Root Mean Square Error (RMSE) >3 kbar for clinopyroxene-orthopyroxene; Wieser et al. 2025), the density of CO_2 fluids trapped within crystals can provide a more sensitive barometer in H_2O-poor ocean island systems assuming the temperature of the system is somewhat constrained (and that inclusions are not modified during suberuptive ascent and/or cooling at the surface).

In sample 04b we identified and measured 30 apparent primary fluid inclusions (FIs) in 8 clinopyroxene crystals, and in sample 03b we found 3 apparent primary FI in 1 clinopyroxene and 1 plagioclases respectively, as well as 7 FIs across 2 secondary trails (1 plagioclase crystal and 1 clinopyroxene crystal; Fig. 11). Of the 43 fluid inclusions, 37 display homogenization temperatures between -9.8°C and -19.1°C. Of the remaining FIs, 3 in sample 04b show clear signs of decrepitation (see Supplementary material) and display T_h values between 27 – 27.1°C (1 FI) and the critical point of CO_2 (2 FIs). Other inclusions with higher homogenization temperatures include one FI in sample 04b (T_h = 4.8 – 4.9°C), and 2 neighboring, apparent primary fluid inclusions in sample 03b (T_h = 17.0 – 17.1°C and T_h = 20.9 – 21.0°C). These 3 FIs are located near the crystal margins, and are among the

ACCEPTED MANUSCRIPT

Downloaded from https://academic.oup.com/petrology/advance-article/doi/10.1093/petrology/egaf031/8102209 by guest on 04 April 2025

largest inclusions in our dataset, making them more susceptible to mechanical re-equilibration during ascent and stalling (Wanamaker and Evans, 1989). As we are interested in determining the long-term storage conditions of these xenoliths prior to ascent in their carrier liquid, we only primarily consider inclusions with no clear signs of decrepitation/re-equilibration (and thus highest densities) in the discussion below.

Assuming the trapped fluids are pure CO_2, the homogenization temperatures indicate fluids densities between 0.98 – 1.03 g/cm^3. Using the median temperature from all clinopyroxene-orthopyroxene thermobarometry calculations for each respective sample we can convert these pure-CO_2 densities into storage pressures ranging from 719 – 802 MPa using the Span and Wagner (1996) EOS in DiadFit (Wieser and DeVitre, 2024). A Monte Carlo approach, accounting for the uncertainty in the measured homogenization temperatures and the equilibration temperatures determined through clinopyroxene-orthopyroxene thermobarometry, suggests uncertainties of +/- 9 MPa for sample 04b and +/- 10 MPa for sample 03b (implemented in DiadFit, Wieser and DeVitre, 2024). Consequently, our data – assuming pure CO_2 fluids – strongly supports the thermobarometry and thermodynamic results discussed above: the Isla Floreana gabbros were stored below the base of the crust, within the lithospheric mantle, prior to entrainment and ascent in their carrier melt.

Converting homogenization temperatures into fluid densities and, ultimately, entrapment/equilibration pressures does, however, require greater examination of the fluid composition. Prior analysis of the H_2O content of Galápagos magmas reveals erupted melt H_2O contents around 0.5 – 1.0 wt% across the southwestern region of the archipelago, with reactive porous flow in crystal mush zones generating anomalously H_2O-rich melt signatures (~2 wt%; Gleeson et al., 2022; Peterson et al., 2017). To account for the possible presence of H_2O in the initial fluid phase we perform calculations using the mixed CO_2-H_2O EOS from Duan and Zhang (2006) implemented in DiadFit (Wieser and DeVitre, 2024). For these calculations we use a fluid X_{H2O} composition of 0.15, representing the maximum X_{H2O} value for any Galápagos magma at mantle

ACCEPTED MANUSCRIPT

Downloaded from https://academic.oup.com/petrology/advance-article/doi/10.1093/petrology/egaf031/8102209 by guest on 04 April 2025

depths (using estimates of melt H_2O contents from the nominally anhydrous mineral analyses of Gleeson et al. 2022). Results demonstrate that incorporation of minor H_2O into these fluids leads to increase in the estimated equilibration pressures, with the median pressure for calculations performed with a X_{H2O} of 0.15 ranging from 821 to 916 MPa. Overall, our calculations indicate that the presence of water increases the estimated pressure by ~14%, further supporting the idea that these gabbros were formed, and were stored, well-below the base of the crust.

As H_2O and CO_2 are immiscible at room temperature, the presence of H_2O will not influence the melting point of a CO_2-rich fluid inclusion. However, our microthermometry results reveal only 15 inclusions – all in sample 04b – with final melting temperatures within 0.2°C of the melting temperature for pure CO_2. Eight other FIs from sample 04b and 3 primary fluid inclusions from sample 03b have final melting temperatures within 1°C of the pure CO_2 melting point, with the remaining inclusions displaying final melting temperatures as low as -60.1°C. In addition, inclusions with low melting temperatures melt over a larger temperature range, with melting initiating as low as -64.5°C in some cases (although the point of melting initiation was difficult to constrain due to the small size of many of these inclusions; ~2 μm). This melting point depression indicates the presence of an additional component (aside from H_2O and CO_2) within the FIs from sample 03b and 04b. Raman spectroscopy did not detect any other Raman-active gaseous species (ruling out N_2, H_2S, SO_2 etc.). Thus we suggest that the observed freezing point depression results from the presence of a Raman-inactive noble gas (e.g., He, Ne, Ar). Although not quite as low as our temperatures here, it is notable that Frezzotti et al. (1992) report melting temperatures of -58.2-56.5°C in xenoliths from Salt Lake Crater, Oahu, which also do not show any Raman-active species other than CO_2.

Using mixed CO_2-He and CO_2-Ar EOS in CoolProp (Bell et al., 2014; Kunz and Wagner, 2012), we can calculate the predicted triple point temperature depression caused by the presence of He or Ar in the 03b and 04b FIs. These calculations suggest that the melting-point depression of the 03b and 04b FIs could result from the presence of up to 1.7 mol% He or 2.7 mol% Ar (or some combination of

ACCEPTED MANUSCRIPT

Downloaded from https://academic.oup.com/petrology/advance-article/doi/10.1093/petrology/egaf031/8102209 by guest on 04 April 2025

780 both). He and Ar proportions up to ~2 mol% have been identified in FIs from picritic lavas and mantle
781 xenoliths collected from La Palma, Canary Islands (Sandoval-Velasquez et al., 2023), supporting this
782 interpretation. We cannot examine the influence of He or Ar on the estimated FI equilibration
783 pressures because converting mixed CO_2-He and CO_2-Ar fluid densities into high-temperature
784 (~1020°C) equilibration pressures is restricted by the temperature range of the mixed EOS
785 calibrations, and the inability of CoolProp to converge on solutions for these mixed fluids above ~300
786 – 400°C. To place a first order assessment on the influence of He and Ar on the estimated pressures
787 we use CoolProp to track the P-T trajectory of isochores for theoretical FIs with a homogenization
788 temperature of -17°C and a range of He and Ar proportions until the maximum convergence
789 temperature for each fluid mixture is reached. The calculations reveal that, for a CO_2-Ar mixed fluid,
790 the presence of 2 mol% Ar lowers the estimated equilibration pressure by <2% (at ~450°C) relative
791 to the isochore of a pure-CO_2 fluid). The presence of He, however, can increase the estimated
792 equilibration pressure by 15% (at a temperature of ~270°C), with this relative offset decreasing with
793 increasing temperature (see Supplementary Information). Therefore, while we cannot directly
794 estimate the equilibration pressure of CO_2-He and CO_2-Ar mixed fluids at the storage temperature of
795 the Isla Floreana gabbros, we conclude that these impurities are likely to have a very minor negative
796 (Ar) or moderate positive (He) influence on the estimated storage pressure derived from the FIs in
797 samples 03b and 04b. As a result, although uncertainties in fluid composition undoubtedly influence
798 the pressure estimates derived from FI measurements, we suggest that the FIs found in samples 03b
799 and 04b confirm that the Isla Floreana gabbros were stored at pressures greater than ~700 MPa and
800 less than ~1 GPa (maximum pressure estimated from CO_2-H_2O calculations combined with the
801 potential influence of He), with a handful of fluid inclusions recording lower pressures due to
802 decrepitation, leakage, re-equilibration, and/or stalling on ascent. Focusing on the fluid inclusions
803 with melting temperatures within 0.1°C of pure CO_2 indicates that the final storage pressure is
804 between 729 MPa (X_{H2O} = 0.0) to 873 MPa (X_{H2O} = 0.15). These pressure estimates closely align with
805 the pressures determined by our thermodynamic calculations where the gabbro phase assemblage

ACCEPTED MANUSCRIPT

Downloaded from https://academic.oup.com/petrology/advance-article/doi/10.1093/petrology/egaf031/8102209 by guest on 04 April 2025

806 is recreated at 750 – 800 MPa and 850 – 1000 MPa (at 1020°C) for the pMELTS and Holland et al.
807 (2018) thermodynamic models, respectively.

808 Converting these pressure estimates into depths using a constant crustal density of 2800 kg/m^3
809 above 16 km and an assumed mantle density of 3200 kg/m^3 below this depth, we constrain the
810 storage depth of the Isla Floreana gabbros to 25.2 – 29.8 km depth (P = 730 – 870 MPa). Critically,
811 the depth of gabbro storage estimated here is significantly greater than the base of the oceanic crust
812 beneath Isla Floreana (~16 km; Feighner and Richards, 1994), indicating that these samples likely
813 formed, and were stored, within the mantle portion of the lithosphere. Therefore, we propose that
814 during the plume-proximal stage of Isla Floreana's volcanic history magma storage was characterized
815 by the presence of "crustal" intrusions (i.e., plagioclase-bearing cumulates) within the lherzolite –
816 harzburgite mantle residue of the Nazca lithosphere.

817 Owing to the small number of samples considered in this study we cannot rule out the possibility
818 that additional samples would reveal the presence of a wider (i.e. more vertically extensive) region
819 of magma storage beneath Isla Floreana. However, we note that a separate set of gabbroic samples
820 analyzed by Lyons et al. (2007) also contain the opx-bearing mineralogy signature that is only stable
821 at sub-Moho pressures (see Supplementary Material). Overall, we find no evidence for magma
822 storage at shallower pressures, either during the plume-proximal or plume-distal period of Isla
823 Floreana's magmatic history, indicating that crustal-level magma storage systems and/or intrusive
824 bodies near the Moho either did not occur or were small and ephemeral and are not represented in
825 the Isla Floreana xenolith populations.

ACCEPTED MANUSCRIPT

Downloaded from https://academic.oup.com/petrology/advance-article/doi/10.1093/petrology/egaf031/8102209 by guest on 04 April 2025

5 IMPLICATIONS FOR VOLCANIC STRUCTURE AND EVOLUTION IN NEAR-RIDGE SETTINGS.

Traditional models for volcanic evolution in ocean island settings are largely based on observations from Hawai'i, and relate changes in the magma storage conditions and erupted compositions of lavas to the position of each volcano relative to the centre of plume upwelling (Clague and Sherrod, 2014; Geist et al., 2014, 1995). As the pressure of magma storage beneath basaltic ocean island volcanoes and the flux of mantle derived magma into the lithosphere have recently been shown to be tightly linked (Baxter et al., 2023; Baxter and Maclennan, 2024; Gleeson et al., 2020a), we would expect to see a systematic increase in the pressure of magma storage as volcanic systems move away from the centre of plume upwelling; i.e., the shield to post-shield transition on Hawai'i (Clague and Sherrod, 2014).

If we consider the modern-day volcanic activity in the Galápagos, the available data appears to fit this prediction very well. Plume-proximal systems that receive the largest flux of mantle-derived magma, such as Isla Fernandina, Volcán Wolf, Volcán Sierra Negra, or Volcán Cerro Azul, are characterized by mid-crustal magma storage regions that feed regular volcanic activity (Bell et al., 2021; Higgins and Stock, 2024; Stock et al., 2018). By contrast, the recent volcanic activity at Isla Floreana, located ~100 – 150 km east-south-east of the centre of Galápagos plume upwelling, is characterized by the high-pressures of magma storage typical of a post-shield, or plume-distal, low melt-flux volcanic centre (Gleeson et al., 2022, 2020a; Fig. 12). From these observations we may have expected the Isla Floreana gabbros, associated with the plume-proximal period of Isla Floreana's magmatic history (Lyons et al., 2007), to record shallow, mid-crustal pressures (similar to the modern-day western Galápagos shield volcanoes). However, our new data indicates that the Isla Floreana gabbros were stored around 10 km below the base of the crust at pressures of ~750 MPa,

ACCEPTED MANUSCRIPT

Downloaded from https://academic.oup.com/petrology/advance-article/doi/10.1093/petrology/egaf031/8102209 by guest on 04 April 2025

849 similar to the pressure estimated for the recent Isla Floreana magmatic system (Gleeson et al., 2022,
850 2020a).

851 As indicated above, a wider region of magma storage – extending to the base of the oceanic crust –
852 cannot be ruled out owing to the small number of samples analyzed. However, our data, combined
853 with the mineralogical signature of other xenolith sample suites from Isla Floreana, clearly indicates
854 that there has been persistent high-pressure magma storage at depths greater than the base of the
855 crust throughout the ~2.5 Myrs of magmatic activity on Isla Floreana. In fact, there is no geochemical
856 or petrological data currently available to indicate that Isla Floreana underwent any period of
857 sustained magma storage within the crustal portion of the lithosphere. The absence of crustal
858 storage beneath Isla Floreana, and other eastern Galápagos volcanic islands, is supported by the
859 absence of shallow-level crustal cumulates detected by recent gravity surveys on other islands in the
860 eastern archipelago (Cleary et al., 2020). We suggest that Isla Floreana has been characterized by a
861 low magma flux (relative to the modern western Galápagos islands of Isabela and Fernandina)
862 throughout its 2.5 Myr history, insufficient to sustain crustal-level magma storage (as links between
863 magma storage depths and mantle derived melt flux have recently been established Baxter et al.,
864 2023; Gleeson et al., 2020a). Importantly, this indicates that the eastern Galapagos volcanic islands
865 cannot be considered as older 'analogues' for the present-day western Galapagos shield volcanoes.
866 The different morphologies and chemical heterogeneity of erupted products, therefore, do not
867 relate to different stages of magmatic evolution, but are likely controlled by differences in the
868 magma flux rate through these volcanoes magmatic histories.

869 The origin of the anomalously low magma flux to the Isla Floreana magma system (and other eastern
870 Galapagos volcanic islands) during its plume proximal stage of volcanic activity could have several
871 origins. Temporal variations in the volume flux of mantle plume systems can occur – and have been
872 documented in Hawai'i – on similar timescales to that investigated here (Morrow and Mittelstaedt,
873 2021; Van Ark and Lin, 2004; Vidal and Bonneville, 2004; Wessel, 2016). However, we suggest that

ACCEPTED MANUSCRIPT

Downloaded from https://academic.oup.com/petrology/advance-article/doi/10.1093/petrology/egaf031/8102209 by guest on 04 April 2025

874 our data supports the recent hypothesis of Cleary et al. (2020), that the persistent low melt flux
875 supplied to the eastern Galapagos islands is related to the changing tectonic setting of the Galápagos
876 mantle plume. Specifically, ~2-2.5 Myrs ago, when Isla Floreana and the other eastern Galápagos
877 volcanic islands were located close to the centre of plume upwelling, the GSC was ~100 km closer to
878 plume stem than it is at the present day. The increased proximity of the plume to the ridge at this
879 time might have allowed more plume material and melt to be diverted northwards towards the
880 ridge axis, causing more distributed volcanism across the Galápagos Platform and lowering the melt
881 flux beneath the islands (Cleary et al., 2020; Gleeson and Gibson, 2021; Harpp and Geist, 2018), an
882 interpretation which is supported by localized crustal thickness anomalies to the north of the GSC
883 (Mittelstaedt et al., 2014). Furthermore, diversion of the plume material northwards, towards to
884 GSC, might have the greatest effect on Isla Floreana owing to its location at the southern margin of
885 the Galápagos Platform. As a result, when the eastern Galápagos islands were formed, Isla Floreana
886 was characterized by a far lower flux of magma into the lithosphere then there is beneath the
887 present-day western Galápagos shield volcanoes of Volcán Cerro Azul or Volcán Sierra Negra.

888 # 6 CONCLUSIONS

889 Our new clinopyroxene trace element data, alongside published isotopic data of similar samples
890 (Lyons et al., 2007), indicates that gabbroic xenoliths found in lava and scoria deposits on Isla
891 Floreana in the southern Galápagos formed at ~2 – 2.5 Ma, when the island was located close to the
892 centre of plume upwelling. Consequently, these samples provide an important insight into the
893 temporal evolution of the Isla Floreana magmatic system, as well as the evolution of the Galápagos
894 Archipelago in a rapidly evolving tectonic setting. Mineral compositions determined by EDS and
895 WDS, alongside analysis of CO_2-density in clinopyroxene- and plagioclase-hosted fluid inclusions, are
896 used to estimate the final storage conditions of these gabbros prior to entrainment and ascent in
897 their carrier melt. Our results indicate that the Isla Floreana gabbros were stored at ~900 – 1050 ^{o}C,

ACCEPTED MANUSCRIPT

Downloaded from https://academic.oup.com/petrology/advance-article/doi/10.1093/petrology/egaf031/8102209 by guest on 04 April 2025

898 with pressures determined by clinopyroxene-orthopyroxene thermobarometry, fluid-inclusion CO_2
899 densities and thermodynamic predictions of phase stability ranging from ~700 MPa to 1 GPa.

900 The storage pressures estimated here indicate that the gabbroic nodules were stored below the
901 base of the crust (~16 km), likely at depths between 25.2 – 29.8 km (although a wider, more
902 vertically extensive magma storage zone extending to the base of the crust remains a possibility).
903 Consequently, our new data indicate that there has been persistent, high-pressure (i.e., lithospheric
904 mantle) magma storage beneath Isla Floreana throughout its 2.5 Myrs of magmatic activity, with no
905 petrological evidence indicating sustained crustal-level magma storage ever occurred, contrary to
906 traditional models for ocean island evolution. In fact, our data indicates that there are no substantial
907 differences between the magma storage conditions estimated for the plume-proximal and plume-
908 distal magmatic systems beneath Isla Floreana (Gleeson et al., 2022, 2020a). In addition, our data
909 indicates that the magma storage conditions beneath the plume-proximal stage of Isla Floreana's
910 magmatic history are very different to the mid-crustal storage regions identified beneath present-
911 day volcanic systems in the western Galápagos (Bell et al., 2021; Stock et al., 2018). As a result, our
912 new data supports recent suggestions that the eastern Galápagos volcanic centres do not represent
913 older analogs of the western Galápagos shield volcanoes (Cleary et al., 2020) but instead are
914 characterized by persistent high-pressure magma storage, possibly resulting from the interaction of
915 the Galápagos mantle plume with the nearby Galápagos Spreading Centre. Consequently, we
916 suggest that the proximity of an ocean island to a nearby ridge segment has a substantial influence
917 on the architecture of magma storage (as plume material and melt may be diverted away from the
918 plume centre and towards the ridge axis) and the evolution of magmatic systems.

919 ACKNOWLEDGEMENTS

920 MG acknowledges the support and funding from the Royal Commission for the Exhibition of 1851
921 Research Fellowship. EDS analyses were performed with support from NSF EAR/IF 2218698. PW and

ACCEPTED MANUSCRIPT

Downloaded from https://academic.oup.com/petrology/advance-article/doi/10.1093/petrology/egaf031/8102209 by guest on 04 April 2025

CJD acknowledge funding from NSF EAR 2217371 and the Rose Hills Innovator Program. MJS acknowledges support from a Charles Darwin and Galápagos Islands Junior Research Fellowship at Christ's College, Cambridge.

DATA AVAILABILITY STATEMENT

All data collected during the preparation of this project, including standard analyses, is available via https://github.com/gleesonm1/GleesonEtAl_JPet_2024_supplement and has been archived using Zenodo (https://doi.org/10.5281/zenodo.12746046). In addition, all supplementary data can be found on EarthChem (https://doi.org/10.60520/IEDA/113382). All Python code used to create the figures presented as part of this manuscript can be found in the Zenodo repository listed above. Other code packages used in this study include: PetThermoTools v0.2.29 (github.com/gleesonm1/PetThermoTools); chemMap v0.0.4 (github.com/gleesonm1/chemMap); Thermobar v1.0.43 (github.com/PennyWieser/Thermobar); DiadFit v1.0.2 (github.com/PennyWieser/DiadFit); mineralML v0.0.0.8 (github.com/sarahshi/mineralML); laserTRAM (github.com/jlubbersgeo/laserTRAM-DB); and pyrolite v0.3.5 (github.com/morganjwilliams/pyrolite/tree/develop). Thermodynamic calculations were performed using alphaMELTS for Python v2.3.1 and MAGEMin_C v1.4.9.

REFERENCES

Argus, D.F., Gordon, R.G., DeMets, C., 2011. Geologically current motion of 56 plates relative to the no-net-rotation reference frame. Geochem. Geophys. Geosystems 12. https://doi.org/10.1029/2011GC003751

Bagnardi, M., Amelung, F., Poland, M.P., 2013. A new model for the growth of basaltic shields based on deformation of Fernandina volcano, Galápagos Islands. Earth Planet. Sci. Lett. 377–378, 358–366. https://doi.org/10.1016/j.epsl.2013.07.016

ACCEPTED MANUSCRIPT

Downloaded from https://academic.oup.com/petrology/advance-article/doi/10.1093/petrology/egaf031/8102209 by guest on 04 April 2025

945 Baxter, R.J.M., Maclennan, J., 2024. Influence of magma flux on magma storage depths along the
946 Reykjanes Ridge. Earth Planet. Sci. Lett. 631, 118633.
947 https://doi.org/10.1016/j.epsl.2024.118633
948 Baxter, R.J.M., Maclennan, J., Neave, D.A., Thordarson, T., 2023. Depth of Magma Storage Under
949 Iceland Controlled by Magma Fluxes. Geochem. Geophys. Geosystems 24, e2022GC010811.
950 https://doi.org/10.1029/2022GC010811
951 Bell, A.F., La Femina, P.C., Ruiz, M., Amelung, F., Bagnardi, M., Bean, C.J., Bernard, B., Ebinger, C.,
952 Gleeson, M., Grannell, J., Hernandez, S., Higgins, M., Liorzou, C., Lundgren, P., Meier, N.J.,
953 Möllhoff, M., Oliva, S.-J., Ruiz, A.G., Stock, M.J., 2021. Caldera resurgence during the 2018
954 eruption of Sierra Negra volcano, Galápagos Islands. Nat. Commun. 12, 1397.
955 https://doi.org/10.1038/s41467-021-21596-4
956 Bell, I.H., Wronski, J., Quoilin, S., Lemort, V., 2014. Pure and Pseudo-pure Fluid Thermophysical
957 Property Evaluation and the Open-Source Thermophysical Property Library CoolProp. Ind.
958 Eng. Chem. Res. 53, 2498–2508. https://doi.org/10.1021/ie4033999
959 Bennett, E.N., Lissenberg, C.J., Cashman, K.V., 2019. The significance of plagioclase textures in mid-
960 ocean ridge basalt (Gakkel Ridge, Arctic Ocean). Contrib. Mineral. Petrol. 174, 49.
961 https://doi.org/10.1007/s00410-019-1587-1
962 Bernard, B., Stock, M.J., Coppola, D., Hidalgo, S., Bagnardi, M., Gibson, S., Hernandez, S., Ramón, P.,
963 Gleeson, M., 2019. Chronology and phenomenology of the 1982 and 2015 Wolf volcano
964 eruptions, Galápagos Archipelago. J. Volcanol. Geotherm. Res. 374, 26–38.
965 https://doi.org/10.1016/j.jvolgeores.2019.02.013
966 Boudoire, G., Brugier, Y.-A., Di Muro, A., Wörner, G., Arienzo, I., Metrich, N., Zanon, V., Braukmüller,
967 N., Kronz, A., Le Moigne, Y., Michon, L., 2019. Eruptive Activity on the Western Flank of Piton
968 de la Fournaise (La Réunion Island, Indian Ocean): Insights on Magma Transfer, Storage and
969 Evolution at an Oceanic Volcanic Island. J. Petrol. 60, 1717–1752.
970 https://doi.org/10.1093/petrology/egz045

ACCEPTED MANUSCRIPT

Downloaded from https://academic.oup.com/petrology/advance-article/doi/10.1093/petrology/egaf031/8102209 by guest on 04 April 2025

971 Bow, C.S., Geist, D.J., 1992. Geology and petrology of Floreana Island, Galapagos Archipelago,
972 Ecuador. J. Volcanol. Geotherm. Res., Special Issue in Honour of Alexander R. McBirney 52,
973 83–105. https://doi.org/10.1016/0377-0273(92)90134-Y
974 Cabral, R.A., Jackson, M.G., Rose-Koga, E.F., Koga, K.T., Whitehouse, M.J., Antonelli, M.A., Farquhar,
975 J., Day, J.M.D., Hauri, E.H., 2013. Anomalous sulphur isotopes in plume lavas reveal deep
976 mantle storage of Archaean crust. Nature 496, 490–493.
977 https://doi.org/10.1038/nature12020
978 Cashman, K.V., Sparks, R.S.J., Blundy, J.D., 2017. Vertically extensive and unstable magmatic systems:
979 A unified view of igneous processes. Science 355, eaag3055.
980 https://doi.org/10.1126/science.aag3055
981 Cherniak, D.J., Liang, Y., 2012. Ti diffusion in natural pyroxene. Geochim. Cosmochim. Acta 98, 31–
982 47. https://doi.org/10.1016/j.gca.2012.09.021
983 Clague, D.A., Bohrson, W.A., 1991. Origin of xenoliths in the trachyte at Puu Waawaa, Hualalai
984 Volcano, Hawaii. Contrib. Mineral. Petrol. 108, 439–452.
985 https://doi.org/10.1007/BF00303448
986 Clague, D.A., Sherrod, D.R., 2014. Growth and degradation of Hawaiian volcanoes (No. 1801–3),
987 Professional Paper. U.S. Geological Survey. https://doi.org/10.3133/pp18013
988 Cleary, Z., Schwartz, D.M., Mittelstaedt, E., Harpp, K., 2020. Dynamic Magma Storage at Near-Ridge
989 Hot Spots: Evidence From New Galápagos Gravity Data. Geochem. Geophys. Geosystems 21,
990 e2019GC008722. https://doi.org/10.1029/2019GC008722
991 Cottaar, S., Lekic, V., 2016. Morphology of seismically slow lower-mantle structures. Geophys. J. Int.
992 207, 1122–1136. https://doi.org/10.1093/gji/ggw324
993 Dayton, K., Gazel, E., Wieser, P., Troll, V.R., Carracedo, J.C., La Madrid, H., Roman, D.C., Ward, J.,
994 Aulinas, M., Geiger, H., Deegan, F.M., Gisbert, G., Perez-Torrado, F.J., 2023. Deep magma
995 storage during the 2021 La Palma eruption. Sci. Adv. 9, eade7641.
996 https://doi.org/10.1126/sciadv.ade7641

ACCEPTED MANUSCRIPT

Downloaded from https://academic.oup.com/petrology/advance-article/doi/10.1093/petrology/egaf031/8102209 by guest on 04 April 2025

997 DeVitre, C.L., Dayton, K., Gazel, E., Pamukçu, A., Gaetani, G., Wieser, P.E., 2023a. Laser heating effect
998 on Raman analysis of CO2 co-existing as liquid and vapor in olivine-hosted melt inclusion
999 bubbles. Volcanica 6, 201–219. https://doi.org/10.30909/vol.06.02.201219
1000 DeVitre, C.L., Gazel, E., Ramalho, R.S., Venugopal, S., Steele-MacInnis, M., Hua, J., Allison, C.M.,
1001 Moore, L.R., Carracedo, J.C., Monteleone, B., 2023b. Oceanic intraplate explosive eruptions
1002 fed directly from the mantle. Proc. Natl. Acad. Sci. 120, e2302093120.
1003 https://doi.org/10.1073/pnas.2302093120
1004 DeVitre, C.L., Wieser, P.E., 2024. Reliability of Raman analyses of CO2-rich fluid inclusions as a
1005 geobarometer at Kīlauea. Geochem. Perspect. Lett. 29, 1–8.
1006 https://doi.org/10.7185/geochemlet.2404
1007 Duan, Z., Zhang, Z., 2006. Equation of state of the H2O, CO2, and H2O–CO2 systems up to 10 GPa
1008 and 2573.15 K: Molecular dynamics simulations with ab initio potential surface. Geochim.
1009 Cosmochim. Acta 70, 2311–2324. https://doi.org/10.1016/j.gca.2006.02.009
1010 Faak, K., Coogan, L.A., Chakraborty, S., 2014. A new Mg-in-plagioclase geospeedometer for the
1011 determination of cooling rates of mafic rocks. Geochim. Cosmochim. Acta 140, 691–707.
1012 https://doi.org/10.1016/j.gca.2014.06.005
1013 Feighner, M.A., Richards, M.A., 1994. Lithospheric structure and compensation mechanisms of the
1014 Galápagos Archipelago. J. Geophys. Res. Solid Earth 99, 6711–6729.
1015 https://doi.org/10.1029/93JB03360
1016 French, S.W., Romanowicz, B., 2015. Broad plumes rooted at the base of the Earth's mantle beneath
1017 major hotspots. Nature 525, 95–99. https://doi.org/10.1038/nature14876
1018 Frezzotti, M.L., Burke, E.A.J., De Vivo, B., Stefanini, B., Villa, I.M., 1992. Mantle fluids in pyroxenite
1019 nodules from Salt Lake Crater (Oahu, Hawaii). Eur. J. Mineral. 4, 1137–1153.
1020 Gao, R., Lassiter, J.C., Barnes, J.D., Clague, D.A., Bohrson, W.A., 2016. Geochemical investigation of
1021 Gabbroic Xenoliths from Hualalai Volcano: Implications for lower oceanic crust accretion and

ACCEPTED MANUSCRIPT

Downloaded from https://academic.oup.com/petrology/advance-article/doi/10.1093/petrology/egaf031/8102209 by guest on 04 April 2025

1022 Hualalai Volcano magma storage system. Earth Planet. Sci. Lett. 442, 162–172.
1023 https://doi.org/10.1016/j.epsl.2016.02.043
1024 Gao, R., Lassiter, J.C., Clague, D.A., Bohrson, W.A., 2022. Evolution of Hawaiian Volcano Magmatic
1025 Plumbing System and Implications for Melt/Edifice and Melt/Lithosphere Interaction:
1026 Constraints from Hualālai Xenoliths. J. Petrol. 63, egac091.
1027 https://doi.org/10.1093/petrology/egac091
1028 Geist, D., Bergantz, G., Chadwick Jr., W.W., 2014. Galápagos Magma Chambers, in: The Galápagos.
1029 American Geophysical Union (AGU), pp. 55–69.
1030 https://doi.org/10.1002/9781118852538.ch5
1031 Geist, D., Howard, K.A., Larson P., 1995. The Generation of Oceanic Rhyolites by Crystal
1032 Fractionation: the Basalt-Rhyolite Association at Volcán Alcedo, Galápagos Archipelago. J.
1033 Petrol. 36, 965–982. https://doi.org/10.1093/petrology/36.4.965
1034 Geist, D., NAUMANN, T.R., STANDISH, J.J., KURZ, M.D., HARPP, K.S., WHITE, W.M., FORNARI, D.J.,
1035 2005. Wolf Volcano, Galápagos Archipelago: Melting and Magmatic Evolution at the Margins
1036 of a Mantle Plume. J. Petrol. 46, 2197–2224. https://doi.org/10.1093/petrology/egi052
1037 Geist, D., White, W.M., Albarede, F., Harpp, K., Reynolds, R., Blichert-Toft, J., Kurz, M.D., 2002.
1038 Volcanic evolution in the Galápagos: The dissected shield of Volcan Ecuador. Geochem.
1039 Geophys. Geosystems 3, 1 of 32–32 32. https://doi.org/10.1029/2002GC000355
1040 Geist, D.J., White, W.M., McBirney, A.R., 1988. Plume-asthenosphere mixing beneath the Galapagos
1041 archipelago. Nature 333, 657–660. https://doi.org/10.1038/333657a0
1042 Ghiorso, M.S., Hirschmann, M.M., Reiners, P.W., Kress III, V.C., 2002. The pMELTS: A revision of
1043 MELTS for improved calculation of phase relations and major element partitioning related to
1044 partial melting of the mantle to 3 GPa. Geochem. Geophys. Geosystems 3, 1–35.
1045 https://doi.org/10.1029/2001GC000217

ACCEPTED MANUSCRIPT

Downloaded from https://academic.oup.com/petrology/advance-article/doi/10.1093/petrology/egaf031/8102209 by guest on 04 April 2025

1046 Gibson, S.A., Geist, D., 2010. Geochemical and geophysical estimates of lithospheric thickness
1047 variation beneath Galápagos. Earth Planet. Sci. Lett. 300, 275–286.
1048 https://doi.org/10.1016/j.epsl.2010.10.002
1049 Gibson, S.A., Geist, D.G., Day, J.A., Dale, C.W., 2012. Short wavelength heterogeneity in the
1050 Galápagos plume: Evidence from compositionally diverse basalts on Isla Santiago. Geochem.
1051 Geophys. Geosystems 13. https://doi.org/10.1029/2012GC004244
1052 Gibson, S.A., Geist, D.J., Richards, M.A., 2015. Mantle plume capture, anchoring, and outflow during
1053 Galápagos plume-ridge interaction. Geochem. Geophys. Geosystems 16, 1634–1655.
1054 https://doi.org/10.1002/2015GC005723
1055 Gleeson, M.L.M., Gibson, S.A., 2021. Insights Into the Nature of Plume-Ridge Interaction and Outflux
1056 of H2O From the Galápagos Spreading Center. Geochem. Geophys. Geosystems 22,
1057 e2020GC009560. https://doi.org/10.1029/2020GC009560
1058 Gleeson, M.L.M., Gibson, S.A., 2019. Crustal controls on apparent mantle pyroxenite signals in
1059 ocean-island basalts. Geology 47, 321–324. https://doi.org/10.1130/G45759.1
1060 Gleeson, M.L.M., Gibson, S.A., Stock, M.J., 2022. Constraints on the behaviour and content of
1061 volatiles in Galápagos magmas from melt inclusions and nominally anhydrous minerals.
1062 Geochim. Cosmochim. Acta 319, 168–190. https://doi.org/10.1016/j.gca.2021.11.005
1063 Gleeson, M.L.M., Gibson, S.A., Stock, M.J., 2020a. Upper Mantle Mush Zones beneath Low Melt Flux
1064 Ocean Island Volcanoes: Insights from Isla Floreana, Galápagos. J. Petrol. 61, egaa094.
1065 https://doi.org/10.1093/petrology/egaa094
1066 Gleeson, M.L.M., Gibson, S.A., Williams, H.M., 2020b. Novel insights from Fe-isotopes into the
1067 lithological heterogeneity of Ocean Island Basalts and plume-influenced MORBs. Earth
1068 Planet. Sci. Lett. 535, 116114. https://doi.org/10.1016/j.epsl.2020.116114
1069 Gleeson, M.L.M., Soderman, C., Matthews, S., Cottaar, S., Gibson, S., 2021. Geochemical Constraints
1070 on the Structure of the Earth's Deep Mantle and the Origin of the LLSVPs. Geochem.
1071 Geophys. Geosystems 22, e2021GC009932. https://doi.org/10.1029/2021GC009932

ACCEPTED MANUSCRIPT

Downloaded from https://academic.oup.com/petrology/advance-article/doi/10.1093/petrology/egaf031/8102209 by guest on 04 April 2025

1072 Grove, T.L., Baker, M.B., Kinzler, R.J., 1984. Coupled CaAl-NaSi diffusion in plagioclase feldspar:
1073 Experiments and applications to cooling rate speedometry. Geochim. Cosmochim. Acta 48,
1074 2113–2121. https://doi.org/10.1016/0016-7037(84)90391-0
1075 Hagiwara, Y., Torimoto, J., Yamamoto, J., 2019. Thermoelastic equilibrium of fluid inclusion–host
1076 mineral systems under homogenization measurement. J. Mineral. Petrol. Sci. 114, 149–154.
1077 https://doi.org/10.2465/jmps.181109b
1078 Hansteen, T.H., Klügel, A., 2008. Fluid Inclusion Thermobarometry as a Tracer for Magmatic
1079 Processes. Rev. Mineral. Geochem. 69, 143–177. https://doi.org/10.2138/rmg.2008.69.5
1080 Harpp, K.S., Geist, D.J., 2018. The Evolution of Galápagos Volcanoes: An Alternative Perspective.
1081 Front. Earth Sci. 6. https://doi.org/10.3389/feart.2018.00050
1082 Harpp, K.S., Geist, D.J., Koleszar, A.M., Christensen, B., Lyons, J., Sabga, M., Rollins, N., 2014. The
1083 Geology and Geochemistry of Isla Floreana, Galápagos, in: The Galápagos. American
1084 Geophysical Union (AGU), pp. 71–117. https://doi.org/10.1002/9781118852538.ch6
1085 Harpp, K.S., Weis, D., 2020. Insights Into the Origins and Compositions of Mantle Plumes: A
1086 Comparison of Galápagos and Hawai'i. Geochem. Geophys. Geosystems 21,
1087 e2019GC008887. https://doi.org/10.1029/2019GC008887
1088 Harpp, K.S., White, W.M., 2001. Tracing a mantle plume: Isotopic and trace element variations of
1089 Galápagos seamounts. Geochem. Geophys. Geosystems 2.
1090 https://doi.org/10.1029/2000GC000137
1091 Herzberg, C., Cabral, R.A., Jackson, M.G., Vidito, C., Day, J.M.D., Hauri, E.H., 2014. Phantom Archean
1092 crust in Mangaia hotspot lavas and the meaning of heterogeneous mantle. Earth Planet. Sci.
1093 Lett. 396, 97–106. https://doi.org/10.1016/j.epsl.2014.03.065
1094 Higgins, O.J., Stock, M., 2024. A new calibration of the OPAM thermobarometer for anhydrous and
1095 hydrous mafic systems.

ACCEPTED MANUSCRIPT

Downloaded from https://academic.oup.com/petrology/advance-article/doi/10.1093/petrology/egaf031/8102209 by guest on 04 April 2025

1096 Hoernle, K., Werner, R., Morgan, J.P., Garbe-Schönberg, D., Bryce, J., Mrazek, J., 2000. Existence of
1097 complex spatial zonation in the Galápagos plume. Geology 28, 435–438.
1098 https://doi.org/10.1130/0091-7613(2000)28<435:EOCSZI>2.0.CO;2
1099 Holland, T.J.B., Green, E.C.R., Powell, R., 2018. Melting of Peridotites through to Granites: A Simple
1100 Thermodynamic Model in the System KNCFMASHTOCr. J. Petrol. 59, 881–900.
1101 https://doi.org/10.1093/petrology/egy048
1102 Holness, M.B., Stock, M.J., Geist, D., 2019. Magma chambers versus mush zones: constraining the
1103 architecture of sub-volcanic plumbing systems from microstructural analysis of crystalline
1104 enclaves. Philos. Transact. A Math. Phys. Eng. Sci. 377, 20180006.
1105 https://doi.org/10.1098/rsta.2018.0006
1106 Hooft, E.E.E., Toomey, D.R., Solomon, S.C., 2003. Anomalously thin transition zone beneath the
1107 Galápagos hotspot. Earth Planet. Sci. Lett. 216, 55–64. https://doi.org/10.1016/S0012-
1108 821X(03)00517-X
1109 Horn, E.L., Taylor, R.N., Gernon, T.M., Stock, M.J., Farley, E.M.R., 2022. Composition and Petrology of
1110 a Mush-Bearing Magma Reservoir beneath Tenerife. J. Petrol. 63, egac095.
1111 https://doi.org/10.1093/petrology/egac095
1112 Jackson, M.G., Hart, S.R., Saal, A.E., Shimizu, N., Kurz, M.D., Blusztajn, J.S., Skovgaard, A.C., 2008.
1113 Globally elevated titanium, tantalum, and niobium (TITAN) in ocean island basalts with high
1114 3He/4He. Geochem. Geophys. Geosystems 9. https://doi.org/10.1029/2007GC001876
1115 Jochum, K.P., Nohl, U., Herwig, K., Lammel, E., Stoll, B., Hofmann, A.W., 2005. GeoReM: A New
1116 Geochemical Database for Reference Materials and Isotopic Standards. Geostand.
1117 Geoanalytical Res. 29, 333–338. https://doi.org/10.1111/j.1751-908X.2005.tb00904.x
1118 Koppers, A.A.P., Becker, T.W., Jackson, M.G., Konrad, K., Müller, R.D., Romanowicz, B., Steinberger,
1119 B., Whittaker, J.M., 2021. Mantle plumes and their role in Earth processes. Nat. Rev. Earth
1120 Environ. 2, 382–401. https://doi.org/10.1038/s43017-021-00168-6

ACCEPTED MANUSCRIPT

Downloaded from https://academic.oup.com/petrology/advance-article/doi/10.1093/petrology/egaf031/8102209 by guest on 04 April 2025

1121 Kunz, O., Wagner, W., 2012. The GERG-2008 Wide-Range Equation of State for Natural Gases and
1122 Other Mixtures: An Expansion of GERG-2004. J. Chem. Eng. Data 57, 3032–3091.
1123 https://doi.org/10.1021/je300655b
1124 Kurz, M.D., Curtice, J., Fornari, D., Geist, D., Moreira, M., 2009. Primitive neon from the center of the
1125 Galápagos hotspot. Earth Planet. Sci. Lett. 286, 23–34.
1126 https://doi.org/10.1016/j.epsl.2009.06.008
1127 Kurz, M.D., Geist, D., 1999. Dynamics of the Galapagos hotspot from helium isotope geochemistry.
1128 Geochim. Cosmochim. Acta 63, 4139–4156. https://doi.org/10.1016/S0016-7037(99)00314-
1129 2
1130 Lamadrid, H.M., Moore, L.R., Moncada, D., Rimstidt, J.D., Burruss, R.C., Bodnar, R.J., 2017.
1131 Reassessment of the Raman CO2 densimeter. Chem. Geol. 450, 210–222.
1132 https://doi.org/10.1016/j.chemgeo.2016.12.034
1133 Lerner, A.H., Wallace, P.J., Shea, T., Mourey, A.J., Kelly, P.J., Nadeau, P.A., Elias, T., Kern, C., Clor, L.E.,
1134 Gansecki, C., Lee, R.L., Moore, L.R., Werner, C.A., 2021. The petrologic and degassing
1135 behavior of sulfur and other magmatic volatiles from the 2018 eruption of Kīlauea, Hawai'i:
1136 melt concentrations, magma storage depths, and magma recycling. Bull. Volcanol. 83, 43.
1137 https://doi.org/10.1007/s00445-021-01459-y
1138 Lissenberg, C.J., MacLeod, C.J., 2016. A Reactive Porous Flow Control on Mid-ocean Ridge Magmatic
1139 Evolution. J. Petrol. 57, 2195–2220. https://doi.org/10.1093/petrology/egw074
1140 Lubbers, J., Kent, A.J., Russo, C., 2021. LaserTRAM-DB: A Time Resolved Analysis Module for the
1141 complete reduction of Laser Ablation Inductively Coupled Plasma Mass Spectrometry data.
1142 Lyons, J., Geist, D., Harpp, K., Diefenbach, B., Olin, P., Vervoort, J., 2007. Crustal growth by magmatic
1143 overplating in the Galápagos. Geology 35, 511–514.
1144 Maclennan, J., 2019. Mafic tiers and transient mushes: evidence from Iceland. Philos. Trans. R. Soc.
1145 Math. Phys. Eng. Sci. 377, 20180021. https://doi.org/10.1098/rsta.2018.0021

ACCEPTED MANUSCRIPT

Downloaded from https://academic.oup.com/petrology/advance-article/doi/10.1093/petrology/egaf031/8102209 by guest on 04 April 2025

1146 Mahr, J., Harpp, K.S., Kurz, M.D., Geist, D., Bercovici, H., Pimentel, R., Cleary, Z., Córdova Aguilar,
1147 M.D., 2016. Rejuvenescent Volcanism on San Cristóbal Island, Galápagos: A Late "Plumer"
1148 2016, V53C-3119.
1149 Matthews, S., Wong, K., Shorttle, O., Edmonds, M., Maclennan, J., 2021. Do Olivine Crystallization
1150 Temperatures Faithfully Record Mantle Temperature Variability? Geochem. Geophys.
1151 Geosystems 22. https://doi.org/10.1029/2020GC009157
1152 Métrich, N., Zanon, V., Créon, L., Hildenbrand, A., Moreira, M., Marques, F.O., 2014. Is the 'Azores
1153 Hotspot' a Wetspot? Insights from the Geochemistry of Fluid and Melt Inclusions in Olivine
1154 of Pico Basalts. J. Petrol. 55, 377–393. https://doi.org/10.1093/petrology/egt071
1155 Mittal, T., Richards, M.A., 2017. Plume-ridge interaction via melt channelization at Galápagos and
1156 other near-ridge hotspot provinces. Geochem. Geophys. Geosystems 18, 1711–1738.
1157 https://doi.org/10.1002/2016GC006454
1158 Mittelstaedt, E., Soule, A.S., Harpp, K.S., Fornari, D., 2014. Variations in Crustal Thickness, Plate
1159 Rigidity, and Volcanic Processes Throughout the Northern Galápagos Volcanic Province, in:
1160 The Galápagos. American Geophysical Union (AGU), pp. 263–284.
1161 https://doi.org/10.1002/9781118852538.ch14
1162 Mittelstaedt, E., Soule, S., Harpp, K., Fornari, D., McKee, C., Tivey, M., Geist, D., Kurz, M.D., Sinton,
1163 C., Mello, C., 2012. Multiple expressions of plume-ridge interaction in the Galápagos:
1164 Volcanic lineaments and ridge jumps. Geochem. Geophys. Geosystems 13.
1165 https://doi.org/10.1029/2012GC004093
1166 Morrow, T.A., Mittelstaedt, E.L., 2021. Quantifying Periodic Variations in Hotspot Melt Production. J.
1167 Geophys. Res. Solid Earth 126, e2021JB021726. https://doi.org/10.1029/2021JB021726
1168 Naumann, T., Geist, D., 2000. Physical volcanology and structural development of Cerro Azul
1169 Volcano, Isabela Island, Galápagos: implications for the development of Galápagos-type
1170 shield volcanoes. Bull. Volcanol. 61, 497–514. https://doi.org/10.1007/s004450050001

ACCEPTED MANUSCRIPT

Downloaded from https://academic.oup.com/petrology/advance-article/doi/10.1093/petrology/egaf031/8102209 by guest on 04 April 2025

1171 Naumann, T.R., Geist, D.J., 1999. Generation of alkalic basalt by crystal fractionation of tholeiitic
1172 magma. Geology 27, 423–426. https://doi.org/10.1130/0091-
1173 7613(1999)027<0423:GOABBC>2.3.CO;2
1174 Neal, C.A., Brantley, S.R., Antolik, L., Babb, J.L., Burgess, M., Calles, K., Cappos, M., Chang, J.C.,
1175 Conway, S., Desmither, L., Dotray, P., Elias, T., Fukunaga, P., Fuke, S., Johanson, I.A.,
1176 Kamibayashi, K., Kauahikaua, J., Lee, R.L., Pekalib, S., Miklius, A., Million, W., Moniz, C.J.,
1177 Nadeau, P.A., Okubo, P., Parcheta, C., Patrick, M.R., Shiro, B., Swanson, D.A., Tollett, W.,
1178 Trusdell, F., Younger, E.F., Zoeller, M.H., Montgomery-Brown, E.K., Anderson, K.R., Poland,
1179 M.P., Ball, J.L., Bard, J., Coombs, M., Dietterich, H.R., Kern, C., Thelen, W.A., Cervelli, P.F.,
1180 Orr, T., Houghton, B.F., Gansecki, C., Hazlett, R., Lundgren, P., Diefenbach, A.K., Lerner, A.H.,
1181 Waite, G., Kelly, P., Clor, L., Werner, C., Mulliken, K., Fisher, G., Damby, D., 2019. The 2018
1182 rift eruption and summit collapse of Kīlauea Volcano. Science 363, 367–374.
1183 https://doi.org/10.1126/science.aav7046
1184 Peterson, M.E., Saal, A.E., Kurz, M.D., Hauri, E.H., Blusztajn, J.S., Harpp, K.S., Werner, R., Geist, D.J.,
1185 2017. Submarine Basaltic Glasses from the Galapagos Archipelago: Determining the Volatile
1186 Budget of the Mantle Plume. J. Petrol. 58, 1419–1450.
1187 https://doi.org/10.1093/petrology/egx059
1188 Putirka, K.D., 2008. Thermometers and Barometers for Volcanic Systems. Rev. Mineral. Geochem.
1189 69, 61–120. https://doi.org/10.2138/rmg.2008.69.3
1190 Reynolds, R.W., Geist, D.J., 1995. Petrology of lavas from Sierra Negra volcano, Isabela Island,
1191 Galápagos archipelago. J. Geophys. Res. Solid Earth 100, 24537–24553.
1192 https://doi.org/10.1029/95JB02809
1193 Riel, N., Kaus, B.J.P., Green, E.C.R., Berlie, N., 2022. MAGEMin, an Efficient Gibbs Energy Minimizer:
1194 Application to Igneous Systems. Geochem. Geophys. Geosystems 23, e2022GC010427.
1195 https://doi.org/10.1029/2022GC010427

ACCEPTED MANUSCRIPT

Downloaded from https://academic.oup.com/petrology/advance-article/doi/10.1093/petrology/egaf031/8102209 by guest on 04 April 2025

1196 Sandoval-Velasquez, A., Rizzo, A.L., Casetta, F., Ntaflos, T., Aiuppa, A., Alonso, M., Padrón, E.,
1197 Pankhurst, M.J., Mundl-Petermeier, A., Zanon, V., Pérez, N.M., 2023. The noble gas signature
1198 of the 2021 Tajogaite eruption (La Palma, Canary Islands). J. Volcanol. Geotherm. Res. 443,
1199 107928. https://doi.org/10.1016/j.jvolgeores.2023.107928
1200 Sanfilippo, A., MacLeod, C.J., Tribuzio, R., Lissenberg, C.J., Zanetti, A., 2020. Early-Stage Melt-Rock
1201 Reaction in a Cooling Crystal Mush Beneath a Slow-Spreading Mid-Ocean Ridge (IODP Hole
1202 U1473A, Atlantis Bank, Southwest Indian Ridge). Front. Earth Sci. 8.
1203 https://doi.org/10.3389/feart.2020.579138
1204 Schwartz, D.M., Harpp, K.S., Mittelstaedt, E.L., 2014. The Interplay Between Deformation and
1205 Volcanism on Santa Cruz Island, Galápagos: A Multidisciplinary Study Using Structural,
1206 Geophysical, and Geochronological Analyses of Faults and Lavas 2014, V41B-4802.
1207 Shi, S.C., Wieser, P.E., Toth, N., Antoshechkina, P.M., Lehnert, K., 2024. MIN-ML: Leveraging Machine
1208 Learning for Probabilistic Mineral Classification in Geochemical Databases. Presented at the
1209 AGU Fall Meetings.
1210 Smith, P.M., Asimow, P.D., 2005. Adiabat_1ph: A new public front-end to the MELTS, pMELTS, and
1211 pHMELTS models. Geochem. Geophys. Geosystems 6.
1212 https://doi.org/10.1029/2004GC000816
1213 Sobolev, A.V., Hofmann, A.W., Kuzmin, D.V., Yaxley, G.M., Arndt, N.T., Chung, S.-L., Danyushevsky,
1214 L.V., Elliott, T., Frey, F.A., Garcia, M.O., Gurenko, A.A., Kamenetsky, V.S., Kerr, A.C.,
1215 Krivolutskaya, N.A., Matvienkov, V.V., Nikogosian, I.K., Rocholl, A., Sigurdsson, I.A.,
1216 Sushchevskaya, N.M., Teklay, M., 2007. The Amount of Recycled Crust in Sources of Mantle-
1217 Derived Melts. Science 316, 412–417. https://doi.org/10.1126/science.1138113
1218 Span, R., Wagner, W., 1996. A New Equation of State for Carbon Dioxide Covering the Fluid Region
1219 from the Triple-Point Temperature to 1100 K at Pressures up to 800 MPa. J. Phys. Chem. Ref.
1220 Data 25, 1509–1596. https://doi.org/10.1063/1.555991

ACCEPTED MANUSCRIPT

Downloaded from https://academic.oup.com/petrology/advance-article/doi/10.1093/petrology/egaf031/8102209 by guest on 04 April 2025

1221 Sparks, R.S.J., Annen, C., Blundy, J.D., Cashman, K.V., Rust, A.C., Jackson, M.D., 2019. Formation and
1222 dynamics of magma reservoirs. Philos. Trans. R. Soc. Math. Phys. Eng. Sci. 377, 20180019.
1223 https://doi.org/10.1098/rsta.2018.0019
1224 Stock, M.J., Bagnardi, M., Neave, D.A., Maclennan, J., Bernard, B., Buisman, I., Gleeson, M.L.M.,
1225 Geist, D., 2018. Integrated Petrological and Geophysical Constraints on Magma System
1226 Architecture in the Western Galápagos Archipelago: Insights From Wolf Volcano. Geochem.
1227 Geophys. Geosystems 19, 4722–4743. https://doi.org/10.1029/2018GC007936
1228 Stock, M.J., Geist, D., Neave, D.A., Gleeson, M.L., Bernard, B., Howard, K.A., Buisman, I., Maclennan,
1229 J., 2020. Cryptic evolved melts beneath monotonous basaltic shield volcanoes in the
1230 Galápagos Archipelago. Nat. Commun. 11, 3767.
1231 Stock, M.J., Taylor, R.N., Gernon, T.M., 2012. Triggering of major eruptions recorded by actively
1232 forming cumulates. Sci. Rep. 2, 731. https://doi.org/10.1038/srep00731
1233 Sun, C., Liang, Y., 2012. Distribution of REE between clinopyroxene and basaltic melt along a mantle
1234 adiabat: effects of major element composition, water, and temperature. Contrib. Mineral.
1235 Petrol. 163, 807–823. https://doi.org/10.1007/s00410-011-0700-x
1236 Sun, C., Lissenberg, C.J., 2018. Formation of fast-spreading lower oceanic crust as revealed by a new
1237 Mg–REE coupled geospeedometer. Earth Planet. Sci. Lett. 487, 165–178.
1238 https://doi.org/10.1016/j.epsl.2018.01.032
1239 Sun, S. -s., McDonough, W.F., 1989. Chemical and isotopic systematics of oceanic basalts:
1240 implications for mantle composition and processes. Geol. Soc. Lond. Spec. Publ. 42, 313–
1241 345. https://doi.org/10.1144/GSL.SP.1989.042.01.19
1242 Van Ark, E., Lin, J., 2004. Time variation in igneous volume flux of the Hawaii-Emperor hot spot
1243 seamount chain. J. Geophys. Res. Solid Earth 109. https://doi.org/10.1029/2003JB002949
1244 Vidal, V., Bonneville, A., 2004. Variations of the Hawaiian hot spot activity revealed by variations in
1245 the magma production rate. J. Geophys. Res. Solid Earth 109.
1246 https://doi.org/10.1029/2003JB002559

ACCEPTED MANUSCRIPT

Downloaded from https://academic.oup.com/petrology/advance-article/doi/10.1093/petrology/egaf031/8102209 by guest on 04 April 2025

1247 Vidito, C., Herzberg, C., Gazel, E., Geist, D., Harpp, K., 2013. Lithological structure of the Galápagos
1248 Plume. Geochem. Geophys. Geosystems 14, 4214–4240.
1249 https://doi.org/10.1002/ggge.20270
1250 Villagómez, D.R., Toomey, D.R., Geist, D.J., Hooft, E.E.E., Solomon, S.C., 2014. Mantle flow and
1251 multistage melting beneath the Galápagos hotspot revealed by seismic imaging. Nat. Geosci.
1252 7, 151–156. https://doi.org/10.1038/ngeo2062
1253 Wanamaker, B.J., Evans, B., 1989. Mechanical re-equilibration of fluid inclusions in San Carlos olivine
1254 by power-law creep. Contrib. Mineral. Petrol. 102, 102–111.
1255 https://doi.org/10.1007/BF01160194
1256 Weis, D., Harpp, K.S., Harrison, L.N., Boyet, M., Chauvel, C., Farnetani, C.G., Finlayson, V.A., Lee,
1257 K.K.M., Parai, R., Shahar, A., Williamson, N.M.B., 2023. Earth's mantle composition revealed
1258 by mantle plumes. Nat. Rev. Earth Environ. 4, 604–625. https://doi.org/10.1038/s43017-
1259 023-00467-0
1260 Wessel, P., 2016. Regional–residual separation of bathymetry and revised estimates of Hawaii plume
1261 flux. Geophys. J. Int. 204, 932–947. https://doi.org/10.1093/gji/ggv472
1262 White, W.M., McBirney, A.R., Duncan, R.A., 1993. Petrology and geochemistry of the Galápagos
1263 Islands: Portrait of a pathological mantle plume. J. Geophys. Res. Solid Earth 98, 19533–
1264 19563. https://doi.org/10.1029/93JB02018
1265 Whitty, R.C.W., Ilyinskaya, E., Mason, E., Wieser, P.E., Liu, E.J., Schmidt, A., Roberts, T., Pfeffer, M.A.,
1266 Brooks, B., Mather, T.A., Edmonds, M., Elias, T., Schneider, D.J., Oppenheimer, C., Dybwad,
1267 A., Nadeau, P.A., Kern, C., 2020. Spatial and Temporal Variations in SO2 and PM2.5 Levels
1268 Around Kīlauea Volcano, Hawai'i During 2007–2018. Front. Earth Sci. 8.
1269 https://doi.org/10.3389/feart.2020.00036
1270 Wieser, P., Petrelli, M., Lubbers, J., Wieser, E., Ozaydin, S., Kent, A., Till, C., 2022. Thermobar: An
1271 open-source Python3 tool for thermobarometry and hygrometry. Volcanica 5, 349–384.
1272 https://doi.org/10.30909/vol.05.02.349384

ACCEPTED MANUSCRIPT

Downloaded from https://academic.oup.com/petrology/advance-article/doi/10.1093/petrology/egaf031/8102209 by guest on 04 April 2025

1273 Wieser, P.E., DeVitre, C., 2024. DiadFit: An open-source Python3 tool for peak fitting of Raman data
1274 from silicate melts and CO2 fluids. Volcanica 7, 335–359.
1275 https://doi.org/10.30909/vol.07.01.335359
1276 Wieser, P.E., Gleeson, M.L.M., Matthews, S., DeVitre, C., Gazel, E., 2025. Determining the pressure-
1277 temperature-composition (P-T-X) conditions of magma storage, in: Anbar, A., Weis, D. (Eds.),
1278 Treatise on Geochemistry (Third Edition). Elsevier, Oxford, pp. 83–151.
1279 https://doi.org/10.1016/B978-0-323-99762-1.00024-3
1280 Williams, M.J., Schoneveld, L., Mao, Y., Klump, J., Gosses, J., Dalton, H., Bath, A., Barnes, S., 2020.
1281 pyrolite: Python for geochemistry. J. Open Source Softw. 5, 2314.
1282 https://doi.org/10.21105/joss.02314
1283 Wilson, D.S., Hey, R.N., 1995. History of rift propagation and magnetization intensity for the Cocos-
1284 Nazca sspreading Center. J. Geophys. Res. Solid Earth 100, 10041–10056.
1285 https://doi.org/10.1029/95JB00762
1286 Wilson, E.L., Harpp, K.S., Schwartz, D.M., Van Kirk, R., 2022. The Geochemical Evolution of Santa Cruz
1287 Island, Galápagos Archipelago. Front. Earth Sci. 10.
1288 https://doi.org/10.3389/feart.2022.845544
1289 Wilson, G., Wilson, T.M., Deligne, N.I., Cole, J.W., 2014. Volcanic hazard impacts to critical
1290 infrastructure: A review. J. Volcanol. Geotherm. Res. 286, 148–182.
1291 https://doi.org/10.1016/j.jvolgeores.2014.08.030
1292
1293

ACCEPTED MANUSCRIPT

Downloaded from https://academic.oup.com/petrology/advance-article/doi/10.1093/petrology/egaf031/8102209 by guest on 04 April 2025

Figure captions

Figure 1 – *Map of the Galápagos Archipelago with the boundaries between different morphological and chemical domains indicated by the red and yellow lines, respectively.* ***A.*** *Topographic and bathymetric map of the Galápagos, data from GEBCO (General Bathymetric Chart of the Oceans). Plate motion estimate taken from Harpp et al. (2014).* ***B.*** *Topographic map of Isla Floreana using high resolution topographic data from the Terra Advanced Spaceborne Thermal Emission and Reflection Radiometer (ASTER) Global Digital Elevation Model (GDEM) Version 3 (ASTGTM) (~30m resolution). Both* ***A.,*** *and* ***B.*** *are created using the World Geodetic Survey (1984) Geographic Coordinate System with an equirectangular projection system. The mean and standard deviation of the* $^{206}Pb/^{204}Pb$ *and* $[Sm/Yb]_n$ *ratios, key chemical parameters that can be used to differentiate between the volcanic systems of Cerro Azul and Isla Floreana, are displayed below alongside the key characteristics defining the chemical progression from west to east along the southern margin of the archipelago. VW – Wolf; CA – Cerro Azul, SN – Sierra Negra, FLO – Isla Floreana, Fer – Isla Fernandina, D – Darwin, A – Alcedo, S – Santiago, SC – Santa Cruz.*

Figure 2 – *Phase maps and associated modal abundances in characteristic gabbro samples.* ***A.*** *Phase map of sample 03b. This sample shows a clear 4 phase mineralogy, with no olivine present.* ***B.*** *Phase proportions, determined by mineralML (Shi et al. 2023), with the associated predicted probability for each analysis shown in the histograms. These confirm the absence of olivine in sample 03b.* ***C.*** *Phase map of sample 09g3. Pixels identified as olivine by MineralML can be seen in the rim regions of orthopyroxene grains.* ***D.*** *Phase proportions confirm the presence of olivine in this sample. Red boxes in panels* ***A.*** *and* ***C.*** *show the areas displayed in Fig. 3.*

Figure 3 – *High-resolution EDS maps of clinopyroxene-orthopyroxene (cpx-opx) grain boundaries.* ***A.*** *EDS map of sample 03b demonstrates a sharp cpx-opx boundary without any breakdown features.* ***B.*** *An EDS linescan across this boundary reveals an absence of chemical zoning in the region near the cpx-opx boundary.* ***C.*** *EDS maps of sample 09g3 demonstrates the presence of an opx-cpx boundary characterised by the presence of an Mg-rich phase and an Si, K, and Na-rich phase.* ***D.&E.*** *Linescans across this boundary reveal the presence of olivine (Mg-rich) and silicate melt (Si-rich) in the rim zone separating the clinopyroxene and orthopyroxene crystals.*

Figure 4 – *Clinopyroxene (and orthopyroxene) compositions from the Isla Floreana Gabbros compared against clinopyroxene data from Volcán Wolf (Stock et al. 2018), chosen as a 'characteristic' western Galápagos volcanic system, and pyroxene analyses from wehrlite xenoliths and clinopyroxene autocrysts from Isla Floreana based on the classification of Gleeson et al. (2020a).* ***A.*** *Pyroxene quadrilateral displaying the narrow range of compositions measured in the Isla Floreana gabbros relative to other datasets from the Galápagos Archipelago (made in Thermobar; Wieser et al. 2022).* ***B. – E.*** *Mg# vs CaO,* Al_2O_3*,* Na_2O*, and* TiO_2 *respectively.*

Figure 5 – *Trace element composition of Isla Floreana clinopyroxenes.* ***A.*** *REE diagram of clinopyroxenes from the Isla Floreana gabbros (colors) and published data from wehrlite xenoliths and clinopyroxene autocrysts (Gleeson et al. 2020a), normalized using the primitive mantle (PM) estimate of Sun and McDonough (1989).* ***B.*** *Eu anomaly (Eu*) vs* $[Ce/Y]_n$*, which is used to demonstrate the degree of incompatible trace element enrichment in each sample.* ***C.*** *The* $[Sm/Yb]_n$ *content of the gabbroic clinopyroxenes is distinct from crystals measured in the wehrlite xenoliths.*

Figure 6 – *Equilibrium melt* $[Sm/Yb]_n$ *compositions calculated from the Isla Floreana clinopyroxenes (****A.****) and published whole-rock data (****B.****). Clinopyroxene trace element data collected in this study (gabbros) and in Gleeson et al. (2020; wehrlites and antecrysts) are converted to equilibrium melt trace element compositions using the REE partitioning model of Sun and Liang (2012) at a temperature of 1150°C and a pressure of 0.5 GPa.*

Figure 7 – *Phase diagrams of samples 03b (****A.****) and 04b (****B.****) constructed in the NCFMASTOCr (Na, Ca, Fe, Mg, Al, Si, Ti, O, and Cr) system. All calculations are performed in PetThermoTools using the pMELTS thermodynamic model (Ghiorso et al. 2002, Gleeson & Wieser, 2024). P-T region where the observed*

ACCEPTED MANUSCRIPT

Downloaded from https://academic.oup.com/petrology/advance-article/doi/10.1093/petrology/egaf031/8102209 by guest on 04 April 2025

*mineralogy is recreated is highlighted in yellow. Also shown are the results of Fluid Inclusion (FI) barometry (solid lines indicate pressures calculated using clinopyroxene-orthopyroxene determined temperatures, dashed lines indicate pressures calculated using Mg-in-plagioclase determined temperatures), and the different subsolidus cooling and burial models used to investigate the phase compositions. For all calculations the Fe^{3+}/Fe_{tot} ratio was set to 0.10. Thicker line indicates the position of the solidus. FI pressures are determined by randomly sampling 1000 temperatures from the clinopyroxene-orthopyroxene thermometry results with the median (circles) and mean ± 2*standard deviation (solid lines) pressure and temperature results shown. Similar calculations are performed using the Mg-in-plagioclase determined temperatures, with the results displayed using the dashed black lines.*

Figure 8 –*Phase proportions and mineral chemistry predicted during cooling and burial from the solidus.* ***A.*** *Mineral proportions predicted during isobaric cooling at 800 MPa. Color scheme as in Fig. 2. Stars indicate the measured mineral proportions derived from the EDS maps.* ***B.*** *Change in clinopyroxene Na_2O contents during isobaric cooling. The grey region represented the range of measured clinopyroxene Na_2O contents in sample 03b.* ***C. & D.*** *Mineral proportions and clinopyroxene chemistry, respectively, predicted during (i) isobaric cooling at 670 MPa, and (ii) burial to 800 MPa.*

Figure 9 – *Plagioclase compositions from the Isla Floreana gabbros compared to data from Volcán Wolf (Stock et al. 2020).* ***A.*** *Feldspar ternary plot produced using the Python3 package Thermobar (Wieser et al. 2022).* ***B.*** *K_2O contents against plagioclase An content.* ***C.*** *Plagioclase MgO contents determined by WDS analysis.* ***D.*** *Temperature calculated from the thermometer of Sun and Lissenberg (2018). All error bars show the 1 sigma analytical uncertainty, with this uncertainty propagated through to the temperature calculations.*

Figure 10 – *Barometric results from the Isla Floreana gabbros (left hand panels) against the estimated Moho pressure and barometric analysis of modern day volcanics in the western (Volcán Wolf) and eastern (Isla Floreana) Galápagos. Modern day estimates are calculated using published clinopyroxene and liquid compositions from Stock et al. (2018) and Gleeson et al. (2020), for Volcán Wolf (orange) and Isla Floreana (blue), respectively. Calculations are performed in Thermobar, using the Neave and Putirka (2017) barometer solved iteratively with equation 33 from Putirka (2008). Melt matching algorithms were performed with the same limits as used in the original papers. Pressure and temperature estimates derived from the Isla Floreana gabbros, which include cpx-opx thermobarometry, Mg-in-plagioclase thermometry, and FI barometry (assuming pure CO_2 fluids), indicate storage of these gabbros at pressures below the Moho. FI pressures are determined by randomly sampling 1000 temperatures from the clinopyroxene-orthopyroxene thermometry results with the median (circles) and mean ± 2*standard deviation (solid lines) pressure and temperature results shown. Similar calculations are performed using the Mg-in-plagioclase determined temperatures, with the results displayed using the dashed black lines.*

Figure 11 – *Analysis of fluid inclusions (FIs) from samples 03b and 04b.* ***A.*** *Comparison of mean homogenization temperature against the final melting temperature. Mixed CO_2-He EOS calculations are used to convert the melting temperature of these inclusions into estimates of the possible He content of these fluid inclusions.* ***B.*** *Comparison of entrapment pressures (at the mean temperature determined by cpx-opx thermobarometry) for different X_{H2O} values (EOS of Span and Wagner (1996) is used when X_{H2O} = 0.0; Duan and Zhang (2006) mixed EOS is used for X_{H2O} = 0.15).* ***C.*** *Example FIs from sample 03b, including the 2 larger inclusions that return anomalously high homogenization temperatures.*

Figure 12 – *Comparison of the tectonic setting of the Galápagos archipelago at 2 – 2.5 Ma (**A.**) and at the present day (**B.**). Reconstruction of the Galápagos Spreading Centre (GSC) is taken from Mittelstaedt et al. (2012), with the right hand panels adapted from Cleary et al. (2020). Schematic diagrams show the proposed increase in melt flux to the western Galápagos due to the increasing plume-ridge interaction distance with time and the smaller volume of plume material (and melt) transported north to the GSC. LAB – Lithosphere Asthenosphere Boundary.*

ACCEPTED MANUSCRIPT

Downloaded from https://academic.oup.com/petrology/advance-article/doi/10.1093/petrology/egaf031/8102209 by guest on 04 April 2025

1389 **Fig. 1.**

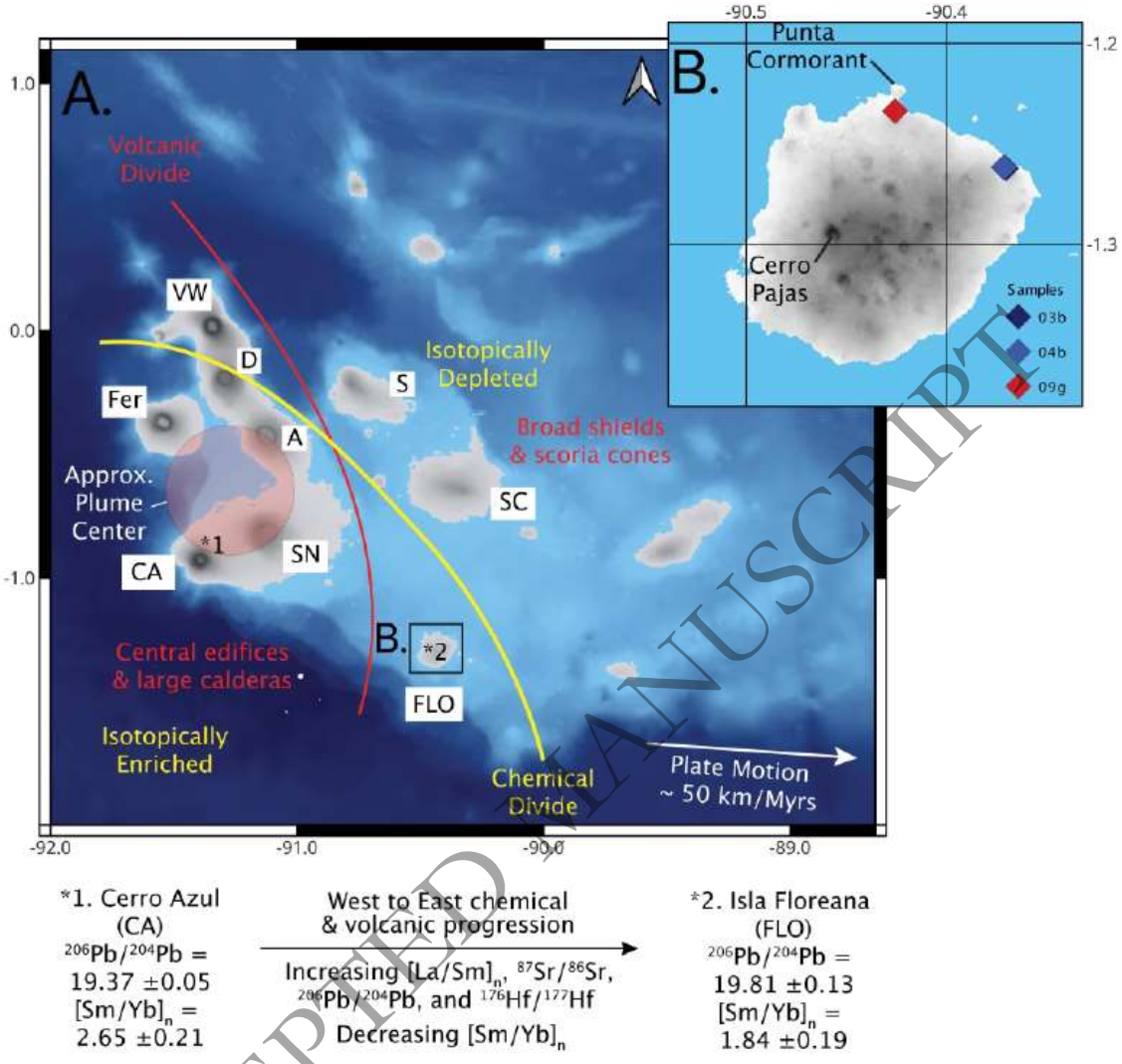

1390

1391

1392

1393

1394

1395

1396

1397

ACCEPTED MANUSCRIPT

Downloaded from https://academic.oup.com/petrology/advance-article/doi/10.1093/petrology/egaf031/8102209 by guest on 04 April 2025

1398 **Fig. 2.**

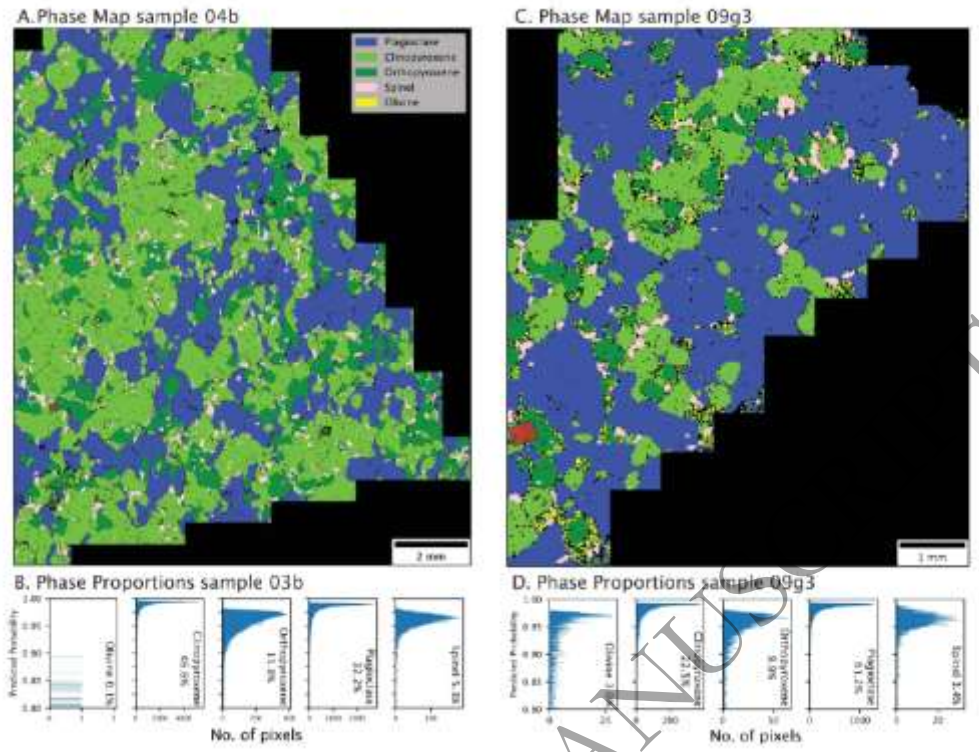

1399

1400

1401

1402

1403

1404

1405

1406

1407

1408

1409

1410

ACCEPTED MANUSCRIPT

Downloaded from https://academic.oup.com/petrology/advance-article/doi/10.1093/petrology/egaf031/8102209 by guest on 04 April 2025

1411 **Fig. 3.**

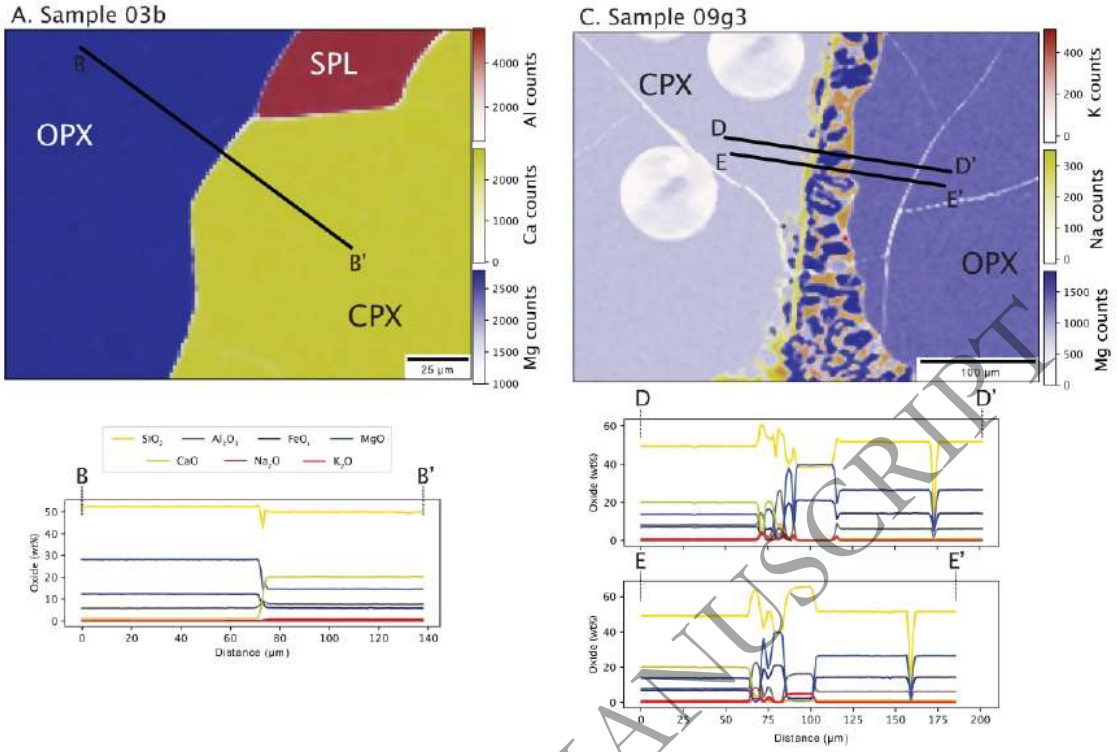

1412

1413

1414

1415

1416

1417

1418

1419

1420

1421

1422

ACCEPTED MANUSCRIPT

Downloaded from https://academic.oup.com/petrology/advance-article/doi/10.1093/petrology/egaf031/8102209 by guest on 04 April 2025

1423 **Fig. 4.**

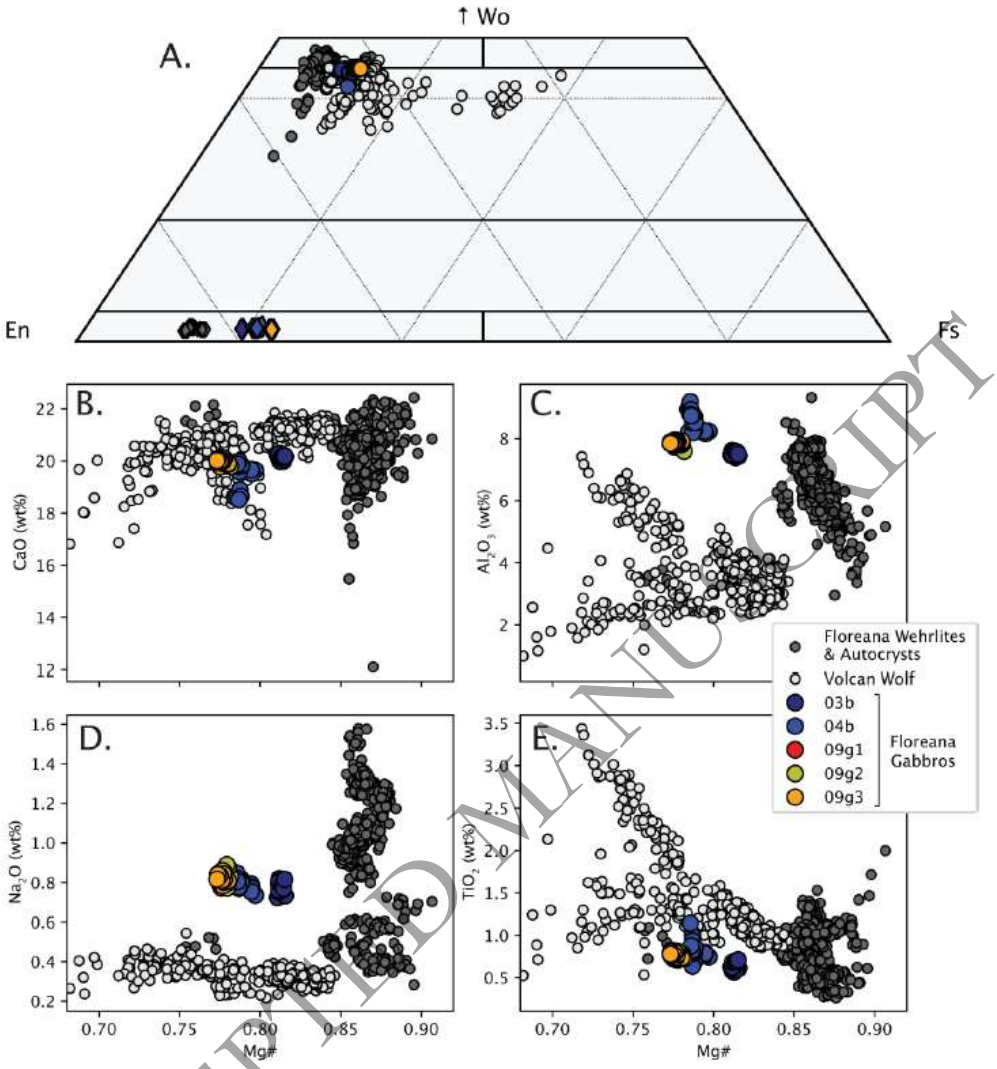

1424

1425

1426

1427

1428

1429

1430

1431

ACCEPTED MANUSCRIPT

Downloaded from https://academic.oup.com/petrology/advance-article/doi/10.1093/petrology/egaf031/8102209 by guest on 04 April 2025

1432 **Fig. 5.**

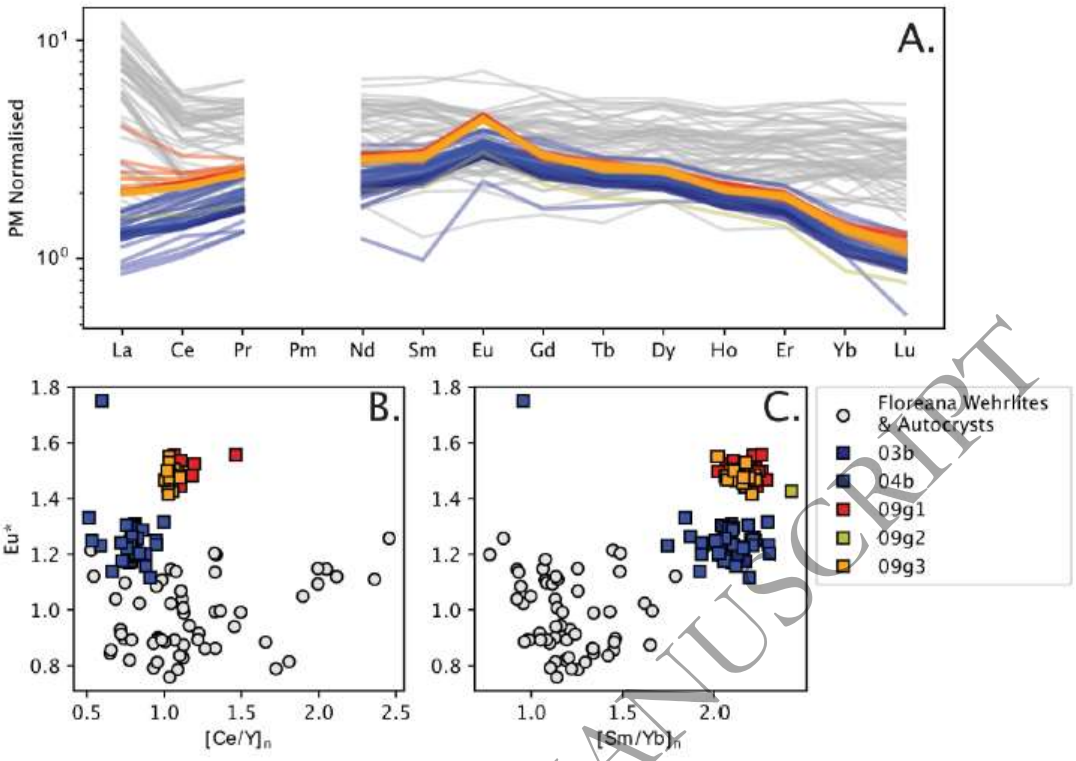

1433

1434

1435

1436

1437

1438

1439

1440

1441

1442

1443

1444

ACCEPTED MANUSCRIPT

Downloaded from https://academic.oup.com/petrology/advance-article/doi/10.1093/petrology/egaf031/8102209 by guest on 04 April 2025

1445 **Fig. 6.**

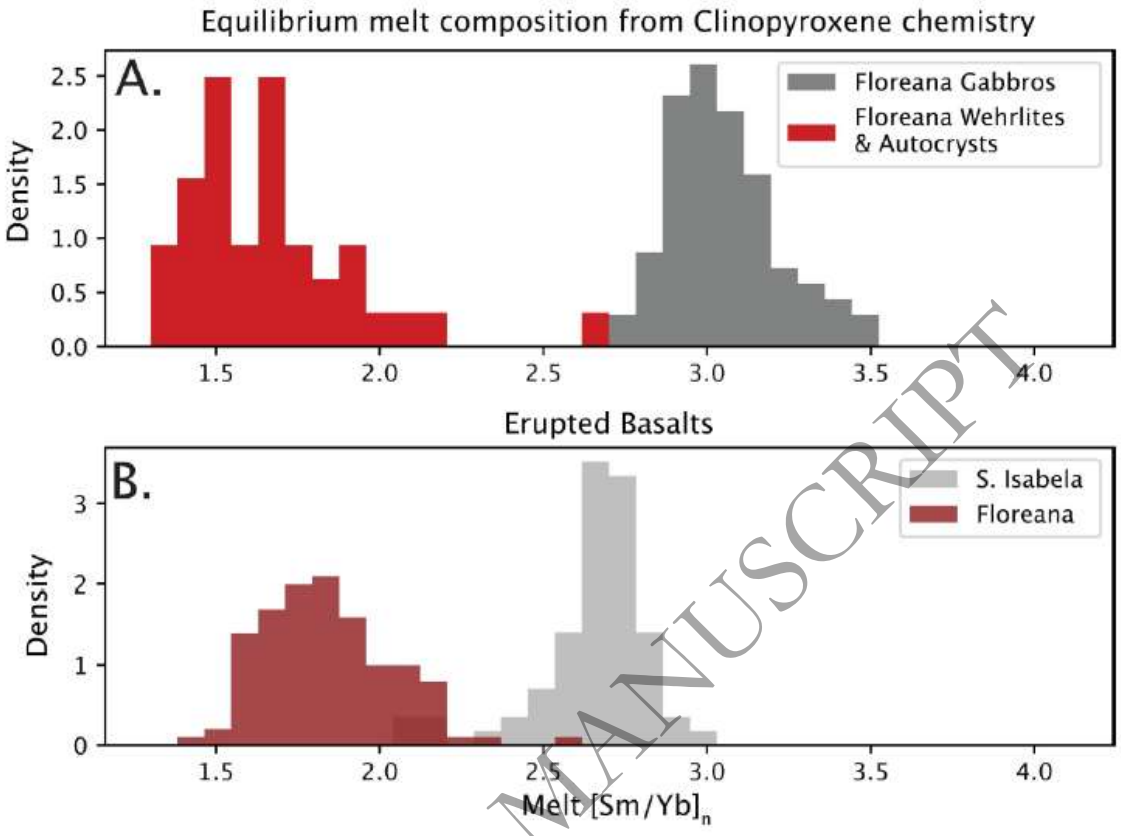

1446

1447

1448

1449

1450

1451

1452

1453

1454

1455

1456

ACCEPTED MANUSCRIPT

Downloaded from https://academic.oup.com/petrology/advance-article/doi/10.1093/petrology/egaf031/8102209 by guest on 04 April 2025

1457 **Fig. 7.**

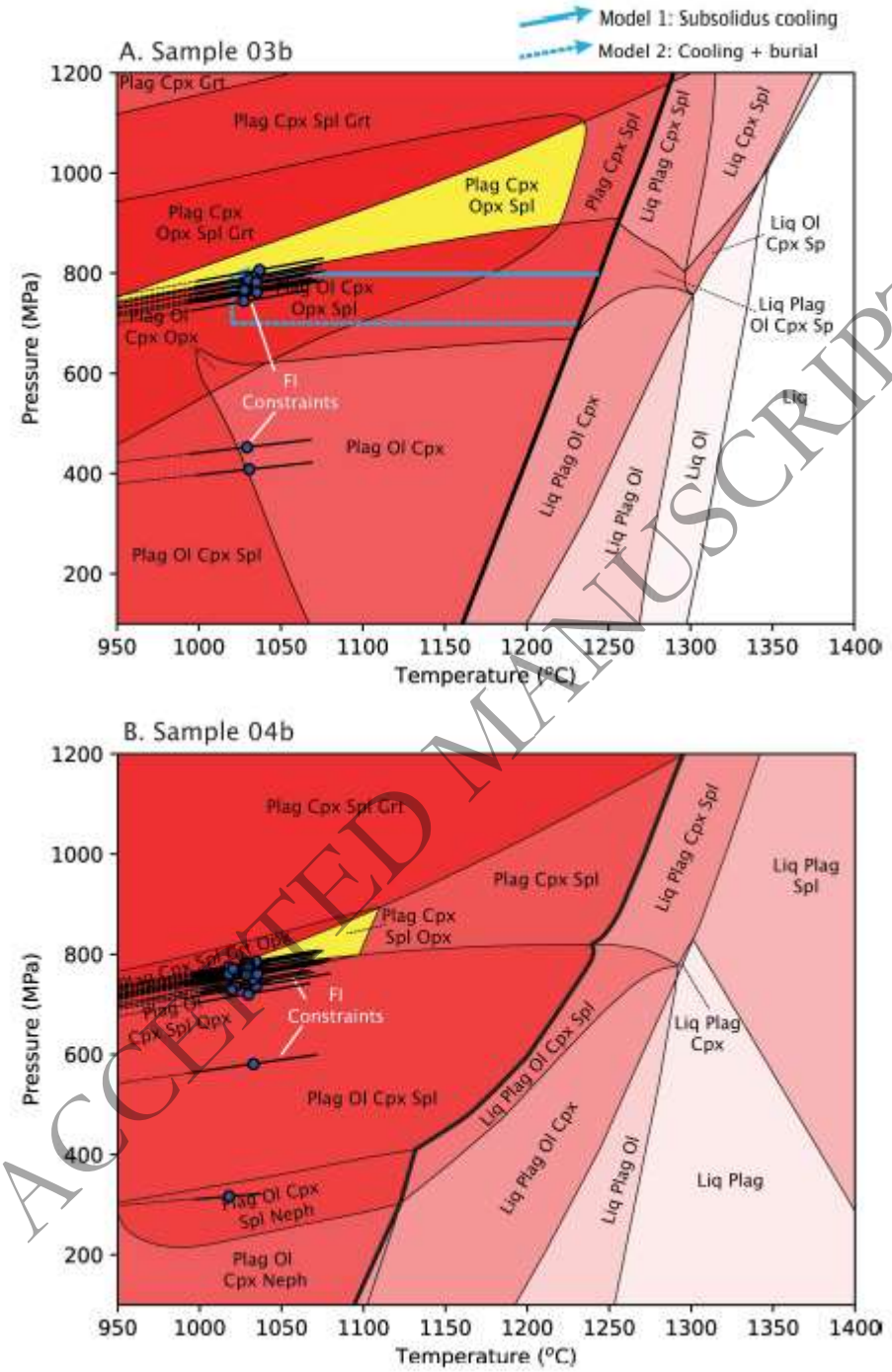

1458

1459

1460

1461

ACCEPTED MANUSCRIPT

Downloaded from https://academic.oup.com/petrology/advance-article/doi/10.1093/petrology/egaf031/8102209 by guest on 04 April 2025

1462 **Fig. 8.**

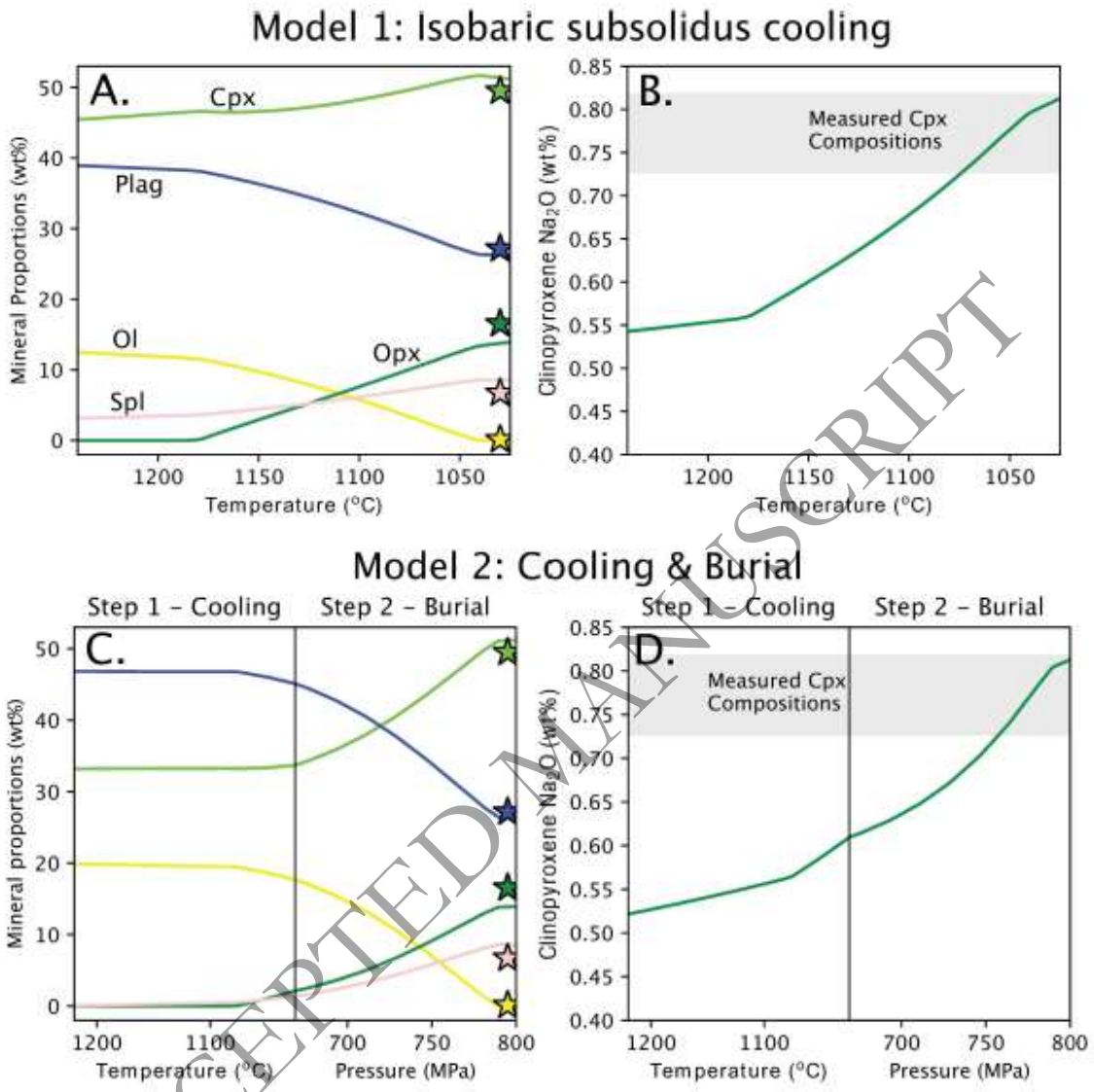

1463

1464

1465

1466

1467

1468

1469

ACCEPTED MANUSCRIPT

Downloaded from https://academic.oup.com/petrology/advance-article/doi/10.1093/petrology/egaf031/8102209 by guest on 04 April 2025

1470 **Fig. 9.**

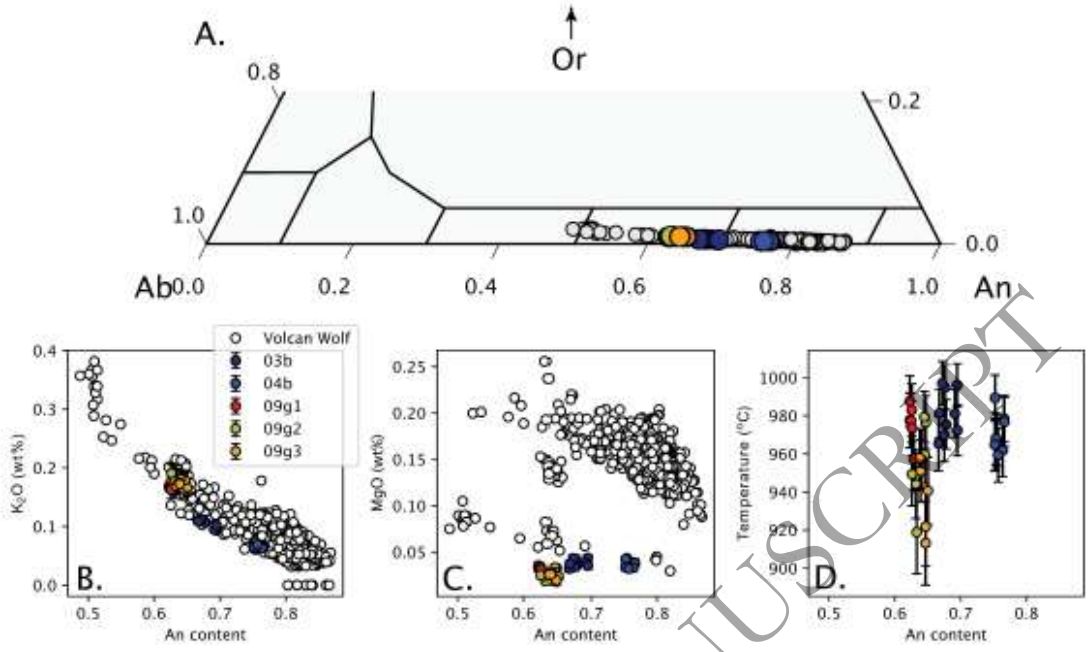

1471

1472

1473

1474

1475

1476

1477

1478

1479

1480

1481

1482

ACCEPTED MANUSCRIPT

Downloaded from https://academic.oup.com/petrology/advance-article/doi/10.1093/petrology/egaf031/8102209 by guest on 04 April 2025

1483 **Fig. 10.**

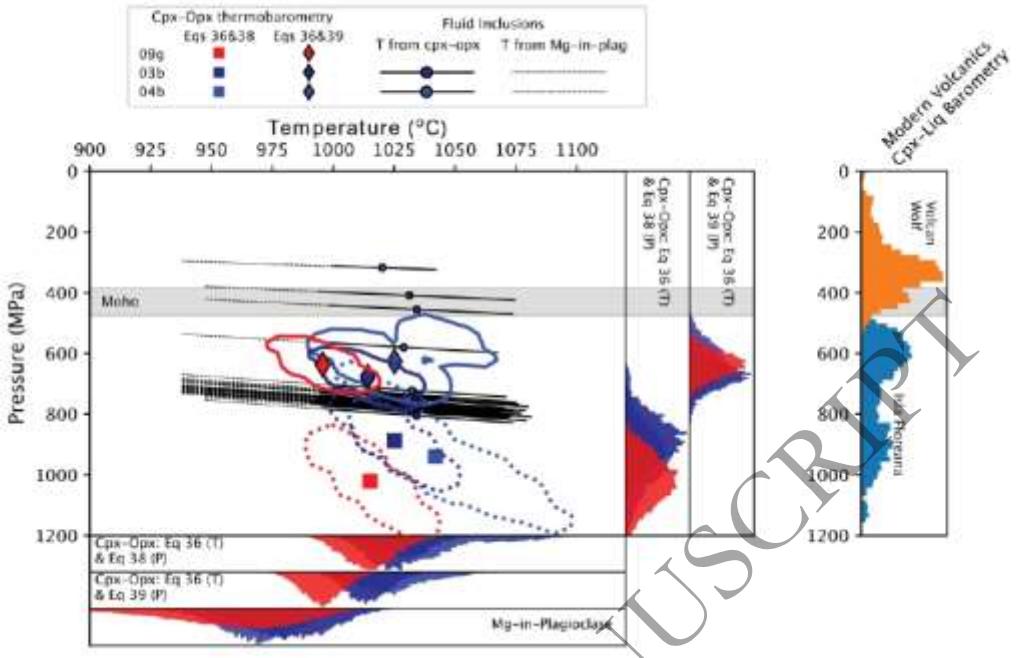

1484

1485

1486

1487

1488

1489

1490

1491

1492

1493

1494

1495

ACCEPTED MANUSCRIPT

Downloaded from https://academic.oup.com/petrology/advance-article/doi/10.1093/petrology/egaf031/8102209 by guest on 04 April 2025

1496 **Fig. 11.**

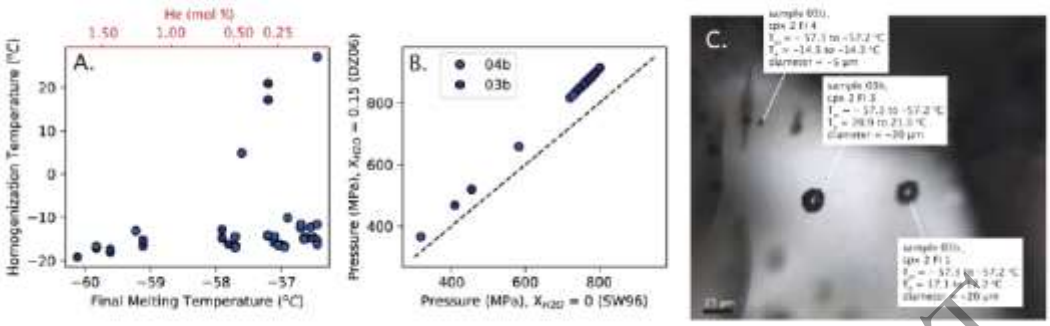

1497

1498

1499

1500

1501

1502

1503

1504

1505

1506

1507

1508

1509

1510

1511

1512

ACCEPTED MANUSCRIPT

Downloaded from https://academic.oup.com/petrology/advance-article/doi/10.1093/petrology/egaf031/8102209 by guest on 04 April 2025

1513 **Fig. 12.**

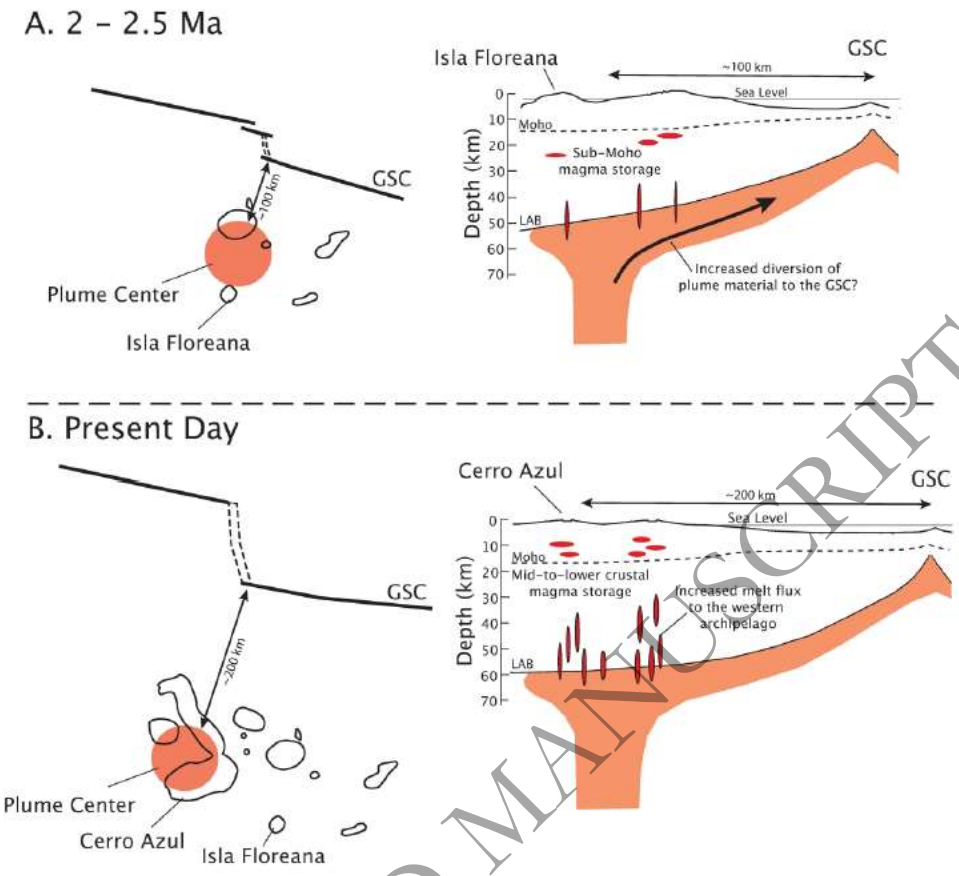

1514

ACCEPTED MANUSCRIPT

Downloaded from https://academic.oup.com/petrology/advance-article/doi/10.1093/petrology/egaf031/8102209 by guest on 04 April 2025

Deltech Furnaces

Sustained operating temperatures to 1800° Celsius

www.deltechfurnaces.com

Gas Mixing System

An ISO 9001:2015 certified company

Custom Vertical Tube

ASME NQA-1 2008 Nuclear Quality Assurance

Standard Vertical Tube

Control systems are certified by Intertek UL508A compliant

Bottom Loading Vertical Tube